



**rijksuniversiteit
 groningen**

ZERNIKE INSTITUTE FOR ADVANCED MATERIALS
UNIVERSITY OF GRONINGEN
THE NETHERLANDS

MASTER THESIS

**ELECTRONIC EXCITATION ENERGY
TRANSPORT IN SELF-ASSEMBLED
MOLECULAR NANOTUBES**

Author:

BJÖRN KRIETE
(s2438445)

Supervisors:

DR. M. S. PSHENICHNIKOV
DR. T. L. C. JANSEN

JUNE 08, 2015

ABSTRACT

Self-assembled tubular aggregates of cyanine dyes are promising candidates for synthetic light harvesting systems as potentially deployable in new generation solar cells due to their remarkably efficient excitation energy transport. In that regard such aggregates are comparable to natural antenna-complexes enhancing photosynthesis in plants, such as Green Sulphur bacteria for instance.

In the frame of this thesis tubular aggregates of the amphiphilic cyanine dye C8S3 were investigated using spectroscopic techniques as well as cryogenic transmission electron microscopy. The latter has proven that upon aggregation of C8S3 molecules in aqueous solution double-walled tubules are formed. The length of these tubes extends up to several μm while maintaining remarkably uniform inner and outer diameters of approximately 6 nm and 15 nm, respectively. Linear absorption spectra reflected this morphological change due to aggregation in form of a strong spectral redshift and the evolution of two narrow peaks referring to the inner and outer cylinder, as predicted by theoretical J-aggregate models. Besides, by comparing fluorescence emission and absorption spectra, strong indications for efficient intercylinder energy transfer could be found. Furthermore, long-term absorption measurements revealed that once the aggregates had formed, they were stable over the course of weeks up to months upon storage. Together with the spectral redshift this finding underlined the proposed strong intermolecular coupling that is responsible for efficient excitation energy migration. An interesting side effect of storage was the formation of bundles consisting of several tubules. Bundling was accompanied by spectral changes, which were not solely explainable by assuming strands of double-walled tubules. Instead, bundles consisted only of the inner cylinder.

To date experiments could not explicitly explain exciton behaviour in tubular C8S3 aggregates. Therefore, the ultimate goal is to establish a well-founded understanding of exciton dynamics in C8S3 aggregates using advanced experimental techniques, such as 2D spectroscopy. Having good control of the system and obtaining reproducible results is the indispensable basis for these experiments.

*Learn from yesterday, live for today, hope for tomorrow.
The important thing is to not stop questioning.*

— Albert Einstein

ACKNOWLEDGMENTS

In the first place I like to thank my master supervisor dr. Maxim Pshenichnikov for making it possible to write this thesis in his group. He was also the one to ask me, whether I would like to join the "Optical Condensed Matter Physics" group and I am glad that I seized this opportunity. I am especially grateful for all the useful discussions we had, which taught me a lot about my research subject and gave me inspirations and new ideas for experiments. I am definitely looking forward to our future collaboration during my PhD.

Next, I like to thank dr. Thomas L. C. Jansen from "Theory of Condensed Matter" group. He kindly agreed to be my second supervisor and assessor of this thesis.

Of course I also like to acknowledge the members of the OCMF group here as well. Having a nice chat in the coffee room or attending social activities together was always very helpful in terms of recovery. In particular I like to thank Oleg Kozlov for his help with the pump probe setup.

Special gratitude also goes to Ben Hesp and Foppe de Haan. They were always available for questions and without their technical expertise solving some experimental problems certainly would have taken twice as long. Here I like to emphasize Ben's patience while introducing me to the streak camera setup and fixing the Hurricane system.

Additionally, I like to acknowledge dr. Marc Stuart and Linda Franken from the electron microscopy group for recording the cryoTEM pictures and helping me with any question I had about cryoTEM. Those magnificent pictures of my aggregates would not have been possible without them.

Last but certainly not least, I like to thank my family and friends. Leisure is undeniably an important part of studying, but without such nice people to spend this time with, it is only half as enjoyable.

Thank you for your support!

CONTENTS

1	INTRODUCTION	1
1.1	Motivation	1
1.2	Outline	3
2	THEORETICAL BACKGROUND	5
2.1	Dimers	5
2.2	Molecular Aggregates	7
2.3	H- & J-Aggregates	9
2.3.1	J-aggregates	9
2.3.2	H-aggregates	11
2.4	Oscillator Strength	12
2.5	Excitons	12
3	MATERIALS AND EXPERIMENTAL METHODS	15
3.1	Materials	15
3.2	Sample Preparation	16
3.3	Experimental Methods	16
3.3.1	Absorption Spectra	16
3.3.2	Fluorescence Emission Spectra	17
3.3.3	Time-Resolved Fluorescence	17
3.3.4	CryoTEM	19
4	RESULTS AND DISCUSSION	21
4.1	Aggregates of C8S3	21
4.2	Absorption Spectra	23
4.2.1	Linear Absorption Spectra	23
4.2.2	Stability of Aggregates	26
4.2.3	Temperature-dependent Absorption Spectra	27
4.3	Fluorescence Emission Spectra	30
4.3.1	Monomers	30
4.3.2	Aggregates	31
4.4	Time-Resolved Fluorescence Spectra	33
4.5	CryoTEM	39
4.5.1	Single Aggregates	40
4.5.2	Bundles	44
4.6	Bundles of C8S3	45
5	CONCLUSION AND OUTLOOK	49
A	APPENDIX	53
	BIBLIOGRAPHY	61

INTRODUCTION

1.1 MOTIVATION

Sustainable energy concepts have experienced rising interest over the past decades, as the overall energy consumption is increasing steadily.[1] A promising approach towards such concepts can be found in mimicking nature, since materials found in primitive marine algae and bacteria are capable of converting solar photons into chemical energy (photosynthesis) at a remarkably high efficiency.[2, 3, 4] In order to utilize their working principles for technological applications, one needs to understand all subunits of the hierarchical structure those photosynthetic systems are composed of: Starting from the individual molecules over supramolecular building blocks to the final close-packed assembly.

While the actual energy conversion process occurs in photosynthetic reaction centres, it is noteworthy that the absorption cross section of the latter is relatively small. Therefore, nature combines them with light harvesting antennae complexes that efficiently absorb photons and funnel the excitation energy (excitons) into the reaction centres. Astonishingly, the overall quantum yield of the mentioned process is close to 100% despite the complexity and sheer size of those systems, as already found in 1952 by Duysens.[5, 6] Furthermore, a detailed review of photosynthetic systems by Cogdell *et al.* has shown that all investigated systems possessed a highly ordered array of pigments, which in turn gives rise to the previously mentioned excitonic character, i.e. the coherent superposition of excited states.[7, 8] Figure 1 provides an illustrative cryoTEM image of such a system.

Taking the high degree of order and the excitonic character as primary requirements for artificial light harvesting systems, a novel design strategy in this field is using derivatives of cyanine dyes, which form low-dimensional supramolecular structures in aqueous solution via self-assembly. To date a vast variety of such dyes has been created.[9, 10] In fact, the tubular structure of these aggregates resembles the morphology of Green Sulphur bacteria, one of the most efficient light-harvesting com-

plexes known nowadays. Top-view cryoTEM images recorded by Ganapathy *et al.* nicely exemplify this structure as shown below.

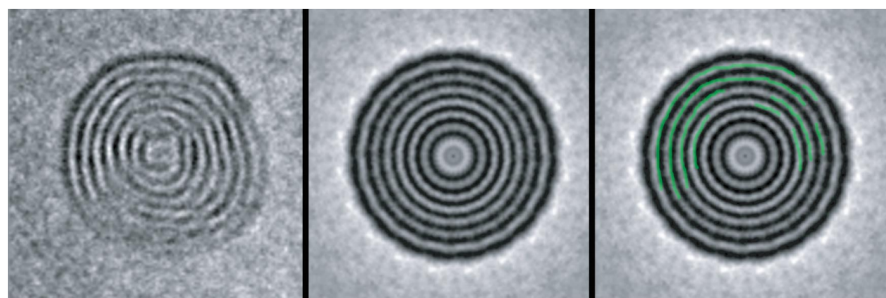


Figure 1: Concentric tubular structure of Green Sulphur bacteria after rotational averaging. Figure taken from the supplementary information of [11].

The aggregates' outstanding optical properties, as characterized by at least one spectrally shifted, narrow transition compared to the monomer spectrum, arise from strong coupling between the individual molecules. As a consequence, electronic excitation via photon absorption leads to the formation of delocalized Frenkel excitons, which migrate along the aggregates over large distances. Recently, Clark *et al.* reported a migration length of 140 nm, which is roughly 5 times as long as the theoretically predicted lower limit of 30 nm.[12, 13] Last but not least, one striking advantage of these systems is that due to self-assembly no effort on the level of molecular engineering is needed once the preparation of the respective aggregates was mastered. Considering all these aspects, cyanine dye derivatives are interesting candidates for artificial light harvesting complexes.

Although the discovery of molecular aggregates dates back almost 100 years [14, 15], even advanced experimental techniques could not resolve molecular packing within those aggregates, neither unravel the nature of excitation energy transport in such structures so far. This lack of insights on the experimental side has restricted the development on the side of molecular and quantum dynamics simulations and, hence, no unified theory that self-consistently describes the exciton behaviour in molecular aggregates exists. Ultrafast 2D spectroscopy offers an opportunity to investigate the correlation between electronic transitions in molecular aggregates on a femtosecond scale.[16, 17] However, before applying this technique, one needs good

understanding and control of the system, which will be in the focus of this thesis.

1.2 OUTLINE

Self-assembled molecular nanotubes of the cyanine dye derivative C8S3 (further details in section 3.1) are in the focus of this thesis. This particular dye forms double-walled cylinders with diameters in the range of tens of nm and lengths exceeding μm s in aqueous solution. In addition to the common methods of characterizing, such as absorption- and fluorescence spectroscopy, samples were also investigated using more elaborate techniques, like time-resolved fluorescence, in order to unravel exciton behaviour in C8S3 aggregates. Further effort was put into understanding the morphology of the tubules by performing cryogenic transmission electron microscopy (cryoTEM) measurements. Insights gained from all these experiments are indispensable for more sophisticated investigations in the future, such as 2D correlation spectroscopy.[16, 17] As the sample preparation turned out to be delicate, special interest was paid to the impact of changes in the environment (temperature, impurities, etc.) on the tubule formation, the effects on the optical properties and, lastly, the stability of the aggregates.

This thesis consists of four separate parts. In Chapter 2, the reader will be introduced to basic background knowledge concerning molecular aggregates in general and the physics of J-aggregates and Frenkel excitons in particular. Subsequently, the sample preparation techniques as well as the experimental methods that were used to acquire the data for this thesis will be discussed in Chapter 3. Then chapter 4 deals with the presentation and discussion of data as obtained from absorption, (time-resolved) fluorescence and cryoTEM measurements. Last but not least, the obtained results will be summarized and accordingly, conclusions will be drawn in Chapter 5. Finally, an outlook to additional investigations will be given.

THEORETICAL BACKGROUND

This chapter deals with the theoretical background knowledge about molecular aggregates, that will be helpful for understanding and interpreting the results as presented in chapter 4. Starting from an elaborate description of the physical dimer, this theory will be generalized to aggregates consisting of a larger quantity of molecules. Subsequently, the two particular cases of J- and H-aggregates will be discussed and, as a closing remark of this chapter, the oscillator strength of optical transitions and excitons in those systems will be addressed.

This chapter follows the book "The Photophysics behind Photovoltaics and Photonics" by *Lanzani*. Further details can be found there.[18]

2.1 DIMERS

To develop a model that describes the optical properties of molecular aggregates, it is a good strategy to start from the simplest case, namely the physical dimer consisting of two interacting single molecules, and then generalize towards higher quantities of interacting molecules.

For the sake of ease, single molecules here are assumed to have only two non-degenerate energy states, one ground state (g) and one excited state (E_i), as shown on the left side of figure 2. Higher-lying energy states of course do exist, but are of minor importance for the considerations presented here. As two molecules approach each other, they start to interact via (weak) dipole-dipole or van der Waals forces, where the latter also include dipole-induced dipole and instantaneous induced dipole-dipole interactions.[19] As a consequence, the energy levels of both molecules are modified, which directly affects the optical characteristics of the dimer compared to its monomeric constituents. The mentioned change can be narrowed down to two quantities: D and V. Firstly, the displacement term D originates from the attractive interaction, such as van der Waals forces for example, of two adjacent molecules. Alternatively, the close proximity of the molecules changes the overall dielectric environment, to which the molecules have to adapt by modifying

their energetical structure. Since both constituents of the dimer are affected equally, a 2-fold degenerate, slightly redshifted excited dimer state is generated.[10, 20] Secondly, V is due the interaction of two adjacent (transition) dipole moments and therefore only applies in the presence of a resonant electromagnetic field, i.e. under illumination for instance. In contrast to D , the mathematical sign and magnitude of V can be different depending on the mutual orientation of the dipole moments, as it will be further quantified in the following paragraphs. Taking both contributions D and V into account, one can write the energy of the resulting two dimer states as follows.

$$E^{\pm} = E_{1,2} - D \pm V. \quad (1)$$

Here E^+ and E^- represent energy states for dipole moment oscillations, which are either in-phase or out-of-phase. Note that at this point it is not possible to generally assign E^+ or E^- to the in- or out-of-phase oscillation, as one also needs to account for geometry in which the dipoles are arranged. For illustration purposes the energy levels discussed so far are plotted in the figure below.

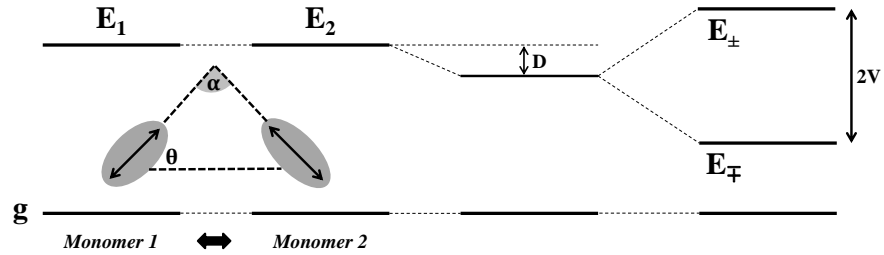


Figure 2: Modification of energy levels due to D and V upon dimerization. The thick black arrow indicates the interaction between the monomers. The inset shows the geometry of two adjacent dipole moments μ_1 and μ_2 in terms of the angles α and θ .

In its most general form the interaction energy V between two dipole moments (μ_1 and μ_2) separated by distance $|r_{12}|$ can be expressed as

$$V = \frac{(\mu_1 \cdot \mu_2)|r_{12}|^2 - 3(\mu_1 \cdot r_{12})(\mu_2 \cdot r_{12})}{|r_{12}|^5}, \quad (2)$$

where symbols in bold are vectors. For a dimer consisting of two identical molecules $|\mu_1|$ can be assumed to be equal to

$|\mu_2|$, thus $|\mu_1| = |\mu_2| = \mu$. Moreover, one can rewrite the scalar products by introducing the angles α and θ (cf. inset of figure 2). Note that in literature θ is also often referred to as slip angle. By applying these considerations to equation 2 one obtains the following, simplified expression:

$$V = \frac{\mu^2}{|r_{12}|^3} (\cos(\alpha) + 3 \cos(\theta) \cos(\theta + \alpha)). \quad (3)$$

The elaborate derivation is given in the appendix, page 53. Since α and θ are the two degrees of freedom of the system, one has to start to distinguish different cases for the mutual orientation of μ_1 and μ_2 at this point, which directly leads to the distinction between H- and J-dimers (or aggregates for a larger number of molecules). This differentiation will be discussed in section 2.3.1 and 2.3.2.

2.2 MOLECULAR AGGREGATES

Increasing the number of interacting molecules from 2 to a large number $N \gg 1$ gives rise to N aggregate energy states. These states are distributed over a band of width $4V$, as depicted by the light grey area in the figure below.

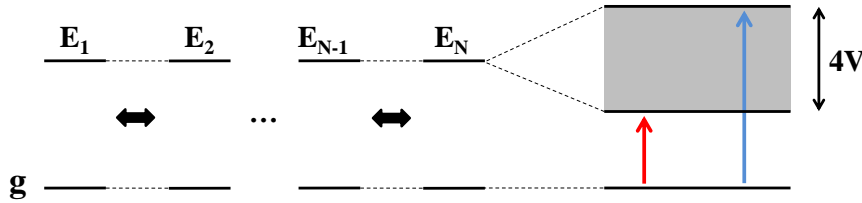


Figure 3: Band of energy levels upon aggregation of N molecules. The contribution of D is neglected as it is a constant shift and affects all N energy levels in the band equally. Thick black arrows indicate the interaction of individual molecules.

Here the maximum and minimum energy states refer to the situation, when all N transition dipole moments are either oscillating in-phase or out-of-phase. Analogous to dimers, it is not yet possible to definitely assign the energy levels to one of the mentioned cases. The red and blue arrow indicate possible optical transitions from the ground state g to the lowest and highest aggregate energy state, respectively. As it will be shown in

the next section, the red transition is allowed for J-aggregates, while the blue transition is allowed for H-aggregates. Intermediate states (counted by index k) between the two extreme cases are formed by a certain share of the dipole moments oscillating in- or out-of-phase compared to the rest. For sufficiently large N one can assume the energy levels to be very close and therefore depict them as a band of states.

One striking difference between dimers and aggregates is the bandwidth of $4V$ instead of $2V$. Taking only nearest-neighbour interactions of the dipole moments into account, the energy states can be described with the formula below.[21, 22]

$$E_k = E_0 + 2V \cos\left(\frac{\pi k}{N+1}\right) \quad (4)$$

Here, V can be specified as $V < 0$ for J-aggregates and $V > 0$ for H-aggregates (cf. section 2.3). In the case of J-aggregates the minimum energy of $E = E_0 - 2|V|$ is reached for $k = 1$, while for $k = N$ one finds $E \approx E_0 + 2|V|$ resulting in the mentioned $4V$ bandwidth. By comparing equation 4 and 1, the cosine dependence of 4 might be surprising on the first glance, but noting that E_k are the eigenvalues of the aggregate Hamiltonian with sinusoidal eigenfunctions explains this observation.[23] However, a rigorous solution to this problem is rather technical and will therefore omitted in this thesis.

Similar to the previous case of dimers, the exact magnitude of V for molecular aggregates depends on the packing of the dipole moments, which determines the mutual orientation of the latter. For illustration, the figure below shows a few possible arrangements for J-type aggregates, i.e. the brickwork, ladder and staircase arrangement.

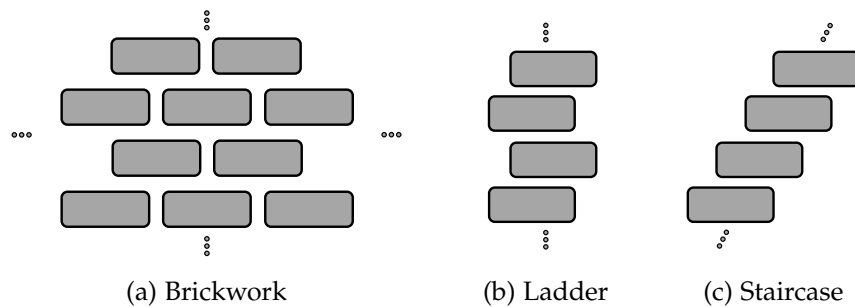


Figure 4: Schematic representation of how molecules in aggregates can be arranged. Here dipole moments are oriented along the long axis of one box. Figure adapted from [10].

As a closing remark, the arrangements in figure 4 only show J-aggregate behaviour, if the dipole moments are oriented along the long axis of one box representing a single molecule. However, in a general case the actual orientation of the dipole moment also depends on the chemical structure and not only on the spatial structure. In other words, one cannot simply associate molecular packing and the arrangement of dipole moments, but also needs to consider the underlying structure.

2.3 H- & J-AGGREGATES

The first discovery of molecular aggregates dates back to the mid 1930s, when E. Jelley and G. Scheibe independently discovered the unique optical properties of pseudoisocyanine (PIC) upon addition of water to a ethanol/PIC solution.[14, 15] As a tribute, molecular aggregates with similar behaviour are still referred to as J- or Scheibe aggregates. Typical for J-aggregates is a spectral redshift of absorption upon aggregation. On the contrary, the name H-aggregate is derived from the word *hypsochromic*, which refers to a spectral blue shift, as characteristic for H-aggregates.

2.3.1 J-aggregates

The characteristic redshift in absorption is the result of the head-to-tail arrangement of the transition dipole moments in the aggregate. Figure 5 illustrates this arrangement for in- and out-of-phase oscillations. Although only two dipole moments are depicted, the principle is identical for larger numbers of interacting molecules.

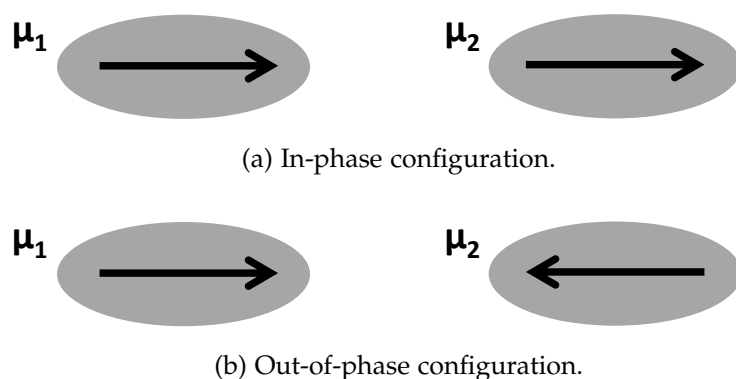


Figure 5: Possible arrangements of the transition dipole moments in J-aggregates.

By applying equation 3 to the two cases shown above, one finds that for case (a) $V < 0$ and for (b) $V > 0$. The detailed calculation is added to the appendix, page 54. Consequently, the associated energy of the in-phase oscillation is smaller than for the out-of-phase oscillation, which means the first relates to the lower energy level in figure 2 and the second to the upper. In order to assess which of these transitions is allowed, one has to compute the vector sum of the dipole moments via equation 5. A more elaborate approach requires solving the dimer Hamiltonian and can be found in [24]. The dimer transition dipole moment μ_D can be written as

$$\mu_D = \frac{1}{\sqrt{2}}(\mu_1 \pm \mu_2). \quad (5)$$

Here $1/\sqrt{2}$ is simply a normalization factor and $\mu_{1,2}$ are molecular dipole moments. Now it is straight forward to see that in (a) the total transition dipole moment equals $\sqrt{2}\mu$, whereas for (b) the transition dipole moment vanishes. According to Fermi's golden rule, the transition in case (b) has zero probability and is therefore forbidden, whereas the first configuration has a finite transition dipole moment and is consequently allowed. As this case refers to the lower energy level, the absorption and accordingly the fluorescence will be shifted towards smaller energies, i.e. redshifted. Further details regarding Fermi's golden rule and general selection rules can be found in quantum mechanics literature, for example [25].

As already implied by figure 4 in the last section, perfect head-to-tail stacking is not required for J-aggregation, but the dipole moments can be tilted and translated to some extent with respect to each other, while $|r_{12}|$ remains approximately constant. Because the system has two degrees of freedom, many different combinations of α and θ lead to the typical redshift and will therefore not be discussed in detail here. However, assuming a coplanar alignment of the dipole moments ($\alpha = 0^\circ$) and vary the angle θ is an interesting scenario, where a transition from J-aggregate behaviour to H-aggregate behaviour occurs. In fact, for $\theta < 54.7^\circ$ the absorption is redshifted, while for $\theta > 54.7^\circ$ the system shows H-aggregate response. This is illustrated in figure 31 in the appendix.

2.3.2 *H*-aggregates

As for J-aggregates, the typical blueshift originates from a particular arrangement of transition dipole moments that is shown below.

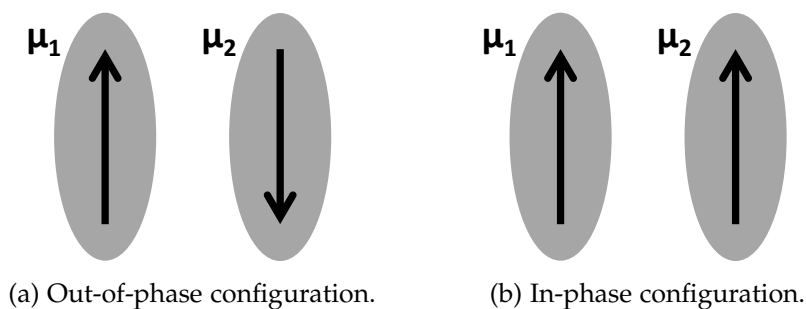


Figure 6: Possible arrangements of the transition dipole moments in H-aggregates. These are also denoted as face-to-face configuration.

Following the same procedure as for the J-aggregates, one finds that here case (a) refers to the lower energy level and case (b) to the upper one. Moreover, one immediately notices that the low energy transition (out-of-phase) is dipole-forbidden, whereas the high energy configuration has a finite transition dipole moment of $\sqrt{2}\mu$ and is therefore allowed. As a result, the aggregate absorption is spectrally blueshifted compared to the absorption of the monomeric constituents. Interestingly, H-aggregates do barely fluoresce, because the lower level is dipole forbidden and the upper level is essentially non-emissive according to Kasha's rule.^[19] All in all, the theory H-aggregates is of minor importance for this thesis, as the investigated system shows J-aggregate behaviour. Nevertheless, for understanding the theory of molecular aggregates it is useful to emphasize the differences of both cases.

Finally, a phenomenological, yet illustrative explanation for the discussed observations can be found in the fact that the separation distance between the dipoles ($|r_{12}|$) is much shorter than the wavelength of the incident electric field (in the visible regime) that drives the oscillations. Hence, adjacent dipoles "see" the same phase of the electric field and only can oscillate in-phase. Depending on the mutual alignment of the dipole moments (head-to-tail or face-to-face), this oscillation can either refer to a redshifted transition (J-aggregates) or a blueshifted transition (H-aggregates).

2.4 OSCILLATOR STRENGTH

For electronic transitions between two states (m and n) in an atom, molecule or aggregate the oscillator strength f_{mn} (or simply f) is often used in spectroscopy to quantify the intensity of this transition. As the number of absorbed or emitted photons determines the intensity, f_{mn} is directly related to the absorption and emission probability.[26] Using Einstein coefficients of absorption and emission, it can be shown that the oscillator strength is proportional to the square of the transition dipole moment μ_{mn} .[27]

$$f_{mn} = \frac{4\pi m_e \nu}{3e^2 \hbar} \mu_{mn}^2 \quad (6)$$

Here m_e is the electron mass, e the elementary charge, \hbar the Planck constant normalized to 2π and ν the frequency associated with the transition. f takes values between 0 and 1, where the latter indicates a strong transition.

For the discussed cases of J- and H-dimers, the net dipole moment of the allowed transitions was equal to $\sqrt{2}\mu$. Thus, the oscillator strength can be calculated to be

$$f \propto \mu_{mn}^2 = (\sqrt{2}\mu)^2 = 2\mu^2, \quad (7)$$

which is twice as high as for the monomer transition ($f \propto \mu^2$). For aggregates consisting of N molecules one finds that $f \propto N\mu^2$ using the same approach as before. Recalling figure 3 one could argue that next to the highest or lowest energy states ($k = 1$) also intermediate states $k = i$ (with $1 < i < N$) contribute to absorption. As a matter of fact, rigorous calculations on J-aggregates have proven that 80% to 90% of the absorption is collected by the $k = 1$ transition and only a small share by the rest.[23, 28] This strongly increased oscillator strength for a small number of transitions combined with a small degree of disorder leads to the characteristic narrow absorption bands.

2.5 EXCITONS

The previous sections addressed optical transitions in dimers and aggregates many times without explicitly explaining the underlying physics. In fact, it is essential to understand the nature of optical transitions in aggregates in order to explain the

remarkable excitation energy transport properties. In view of the framework of this thesis, the focus of the following section will be on J-aggregates.

Due to intermolecular coupling of the individual sites in J-aggregates, the absorption of a photon leads to the formation of a delocalized excited state also referred to as exciton. Among different exciton models, each based on the underlying class of material, the Frenkel exciton model has proven itself to be an accurate model for J-aggregates, as these generally consist of organic compounds featuring a low dielectric constant ϵ .^[21, 29, 30] An illustrative picture for such an exciton is a tightly bound electron-hole pair, where an electron is promoted to the excited state, while a hole resides in the ground state. Accordingly, a good estimation for the binding energy of such an exciton can be found in the energy that is required to separate those charges by overcoming the Coulomb attraction.

However, from this point of view it is difficult to visualize the delocalization of the exciton. Instead, another possible representation of an exciton is as a wavepacket Ψ with a group velocity v_g and an effective mass m^* . These wavepackets are formed via the coherent superposition of excitonic states.^[31] Because the amplitude square $|\Psi|^2$ describes the probability of finding an excited state on a certain site, the delocalization picture is much more instructive now. Figure 7 depicts this situation in a very schematic fashion.

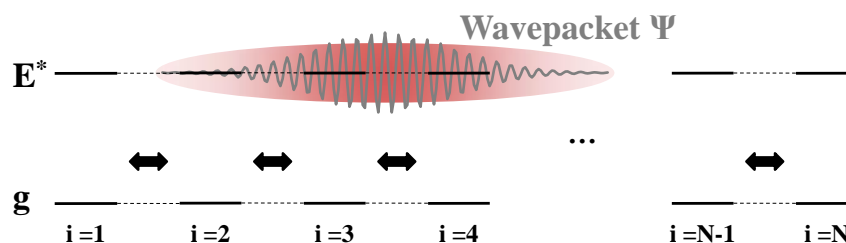


Figure 7: Delocalization of an exciton wavepacket in an aggregate. Index i counts the molecular sites; black arrows indicate intermolecular interaction. g is the ground state and E^* the excitonic state.

Excitation energy migration occurs via the propagation of the wavepacket with group velocity v_g , which is determined by the energy dispersion relation $E(k)$ via $v_g = \frac{1}{\hbar} \frac{\partial E}{\partial k}$. Here, one relevant limitation for the migration length of an exciton is its lifetime, which describes the timespan between excitation and (de-

pending on the considered system) radiative or non-radiative decay.

It is important to notice that fully resonant energy transport is rather exceptional for a system. Due to mechanisms that impede the resonant excitation transfer interaction, such as internal vibrations or other interactions with the environment, the exciton might be localized on one monomer and is only able to migrate along the aggregate via an incoherent hopping process.^[24] The Förster model as proposed in 1948 is one possible model to describe the latter.^[32] In this model excitation energy is transferred between two chromophores separated by distance R with an efficiency that scales with R^{-6} . Another important factor that determines the energy transfer efficiency is the spectral overlap of the donor emission spectrum and the acceptor absorption spectrum. If this overlap is weak due to a strong Stokes shift, the efficiency will be low and vice versa for a large overlap.^[33] Taking these factors into account, it is therefore not surprising that the Förster resonant energy transfer (FRET) can be assumed to be less efficient compared to the initially discussed energy transfer via wavepacket migration.

In reality one usually deals with a mix of both models meaning that experimentally determined diffusion lengths are situated somewhere in between the extremes of fully coherent transport and fully incoherent transport.

MATERIALS AND EXPERIMENTAL METHODS

This chapter provides a summary of the material specifications, the sample preparation and the various experimental techniques deployed for characterization.

3.1 MATERIALS

The dye investigated in this work 3,3'-bis(2-sulfopropyl)-5,5',6,6'-tetra-chloro-1,1'-dioctylbenzimidacarbocyanine (abbreviated as C8S3) was purchased from FEW Chemicals GmbH (Wolfen, Germany) and used as received. A detailed description of the synthesis as well as the purification can be found in [34]. According to the supplier, the molecular mass of C8S3 amounts to $902.79 \text{ g mol}^{-1}$. The maximum absorption of the pure dye dissolved in methanol occurs at 520 nm and the molar extinction coefficient is equal to $1.46 \times 10^5 \text{ l mol}^{-1} \text{ cm}^{-1}$ at this wavelength. The chemical structure of C8S3 is shown in the figure below.

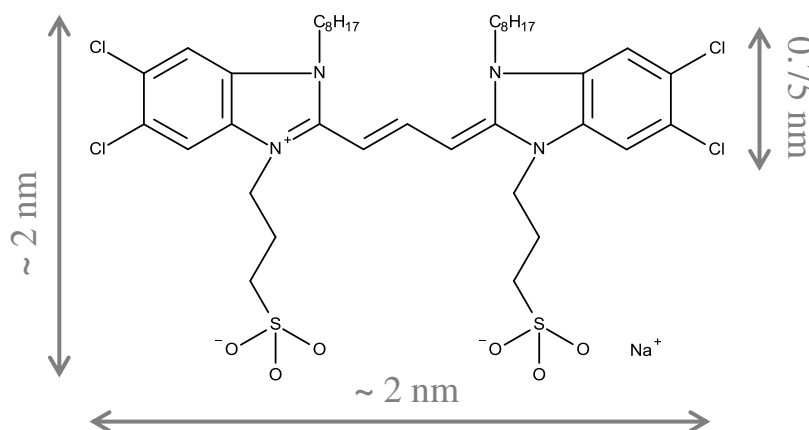


Figure 8: Chemical structure of C8S3. The hydrogen atoms are not displayed.

For some considerations in following chapters it will be useful to have a rough estimation of the physical size of a monomer. According to von Berlepsch *et al.* the geometrical dimensions of a chromophore are approximately $2.00 \text{ nm} \times 0.75 \text{ nm} \times 0.40 \text{ nm}$, where 2.00 nm refers to the length between the two dichloroben-

imidazole moieties, as depicted in figure 8.[35] Concerning the size of the whole molecule including its side chains, simple geometric considerations in form of adding up bond lengths yield a value of approximately 2 nm, which is in line with the value found by Prokhorov *et al.*[36] Although there are no detailed studies investigating the monomer size of C8S3, one can find values for similar molecules, that coincide with the mentioned figures.[37]

3.2 SAMPLE PREPARATION

Sample solutions were prepared using two different ways, i.e. either via the direct route or the alcoholic route. For the direct route a small amount of the dye was directly dissolved in deionized water (Sigma Aldrich). As the pure dye is hardly soluble in water, stirring at room temperature for at least 24 h was necessary. For the alcoholic route the dye was initially dissolved in pure methanol (Lab-Scan Analytical Sciences) yielding a C8S3 stock solution of $1.75 \times 10^{-3} \text{ mol l}^{-1}$. In order to initiate the aggregation of single dye molecules, 0.3 ml stock solution were mixed with 1.7 ml deionized water and left 24 h for aggregation. Stirring was not necessary for that procedure. Either way the sample solutions were stored in the dark to avoid photodegradation. In both cases the final dye concentration of the sample solution was equal to approximately $2.5 \times 10^{-4} \text{ mol l}^{-1}$.

3.3 EXPERIMENTAL METHODS

3.3.1 Absorption Spectra

Linear absorption spectra were recorded using a PerkinElmer Lambda 900 UV/VIS/NIR Spectrometer and fused silica cuvettes with a thickness of 1 mm. Due to their high concentration, stock solutions were strongly diluted with methanol by approximately factor 5 before recording the absorption spectra. In case of sample solutions strong dilution was not necessary. However, the samples were diluted (using the same water as for the preparation) by approximately factor 2 to ensure a sufficiently low optical density (OD) for the spectrometer. In order to minimize light exposure of the dye, measurements were executed within 10 minutes after the preparation of the cuvettes. Stock solutions were investigated in the wavelength range from 350 nm to 700 nm, whereas for sample solutions the range was

400 nm to 800 nm. In both cases the step width was chosen to be 0.5 nm and the integration time per step was set to 0.04 s.

Absorption spectra are depicted as optical density (OD) or extinction ϵ versus wavelength λ . The optical density is defined via the Lambert-Beer law,

$$I_t = I_0 10^{-OD}, \quad (8)$$

where I_0 is the incident and I_t is the transmitted light intensity. Because I_t also depends on the sample thickness l and the dye concentration c one can further specify OD by writing:

$$OD = \epsilon cl. \quad (9)$$

Equation 9 shows that ϵ is OD normalized to sample thickness and concentration. Both quantities (OD and ϵ) will be used in this thesis.

3.3.2 Fluorescence Emission Spectra

Fluorescence emission spectra were recorded using a Perkin Elmer LS50B Luminescence Spectrometer and fused silica cuvettes with a thickness of 1 mm. The emitted photons were collected in a front face geometry. For these measurements the sample solutions needed to be strongly diluted down to a concentration of about $7.5 \times 10^{-6} \text{ mol l}^{-1}$. Dilution was crucial, as for high concentrations reabsorption of emitted photons would modify the spectrum spectrally and certain features would not be distinctively observable. As for absorption spectra, measurements were executed within 10 minutes after the preparation of the cuvettes to minimize light exposure of the samples. In order to obtain the highest resolution, the slit widths were adjusted to a value of 2.5 nm for excitation and emission slits, respectively. If not differently stated the excitation wavelength for sample solutions was set to 560 nm and the measured wavelength range was between 570 nm and 700 nm.

3.3.3 Time-Resolved Fluorescence

Time-resolved fluorescence measurements were performed on strongly diluted sample solution ($7.5 \times 10^{-6} \text{ mol l}^{-1}$) to avoid reabsorption of emitted photons. The experiments were carried

out under ambient conditions using a streak camera system with synchro-scan unit from Hamamatsu. The system could operate at four different time bases, each offering a different maximum time window for investigation. Generally, the faster the time base was, the better was the temporal resolution. Choosing the appropriate time base for a sample is a trade-off between fluorescent lifetime to be examined and resolution. To excite the sample the output of a frequency tunable Ti:Sapphire laser (Mira 900, Coherent) generating 120 fs pulses at a repetition frequency of 80 MHz was focused into an optical fiber producing a broad spectrum of wavelengths due to nonlinear processes. A suitable excitation wavelength was picked subsequently by means of a narrow bandpass filter with a centre wavelength of 550 nm and a FWHM of 10 nm. In order to separate the actual fluorescence signal from scattered excitation light, a longpass filter with cut-off at 570 nm was used. However, some portion of the scattered excitation light leaked through the filter and could be used to determine the time resolution of the system, which was equal to 5.2 ps for the fastest time base. Spectral resolution of the fluorescence signal was achieved by using a polychromator (CHROMEX) in front of the streak camera, which was calibrated using a mercury argon lamp (Oceans Optics) prior to actual measurements. As photodegradation of the aggregates turned out to be a problem, sample solutions were stirred throughout the entire experiment. Data was obtained in photon counting mode.

It is important to realize that the setup incorporates a large number of optical elements, such as lenses, fibers and filters, each with an inherent dispersion, that was not compensated for. Despite the temporal broadening of the excitation pulse, that is no longer in the fs, but rather ps range, the transients of the fluorescence response are also temporally modified. In fact, the dispersion causes temporal retardation of spectral components up to ps meaning that they arrive at the CCD screen of the streak camera with a certain delay. The significance of this effect increases as the spectral interval to be investigated becomes broader, because the refractive index n is a function of wavelength λ . Of course, one can compensate for that by carefully calibrating the zero time line. However, as no strong indications for dispersion related distortions of the signal were observed, this procedure was omitted in this thesis.

3.3.4 CryoTEM

The samples for cryoTEM, which is a short term for cryogenic transmission electron microscopy, were prepared following the route as presented by Didraga *et al.*[29] A droplet of the sample solution (approximately 3 μ l) was placed on a copper grid with holey carbon film (quantifoil 3.5/1), which was first hydrophilized using a glow discharging device. In order to obtain an ultrathin layer of the solution in the range of 100 nm, the excess fluid was blotted off for 4 s. Immediately afterwards the grid was vitrified in liquid ethane at its freezing point (-184°C) with a Vitrobot plunging device (FEI, Eindhoven, The Netherlands). This procedure is crucial as one needs to prevent the water from forming crystalline ice during freezing, but amorphous ice instead. Therefore, liquid nitrogen is not suitable for the mentioned process due to its poor thermal conductivity and low heat capacity. Under continuous cooling in a cryo-transfer holder (Gatan model 626) at liquid nitrogen temperature (-196°C), the samples were then transferred into a Tecnai 20 transmission electron microscope with LaB₆ cathode operated at 200 kV. Micrographs were recorded with a slow scan CCD camera using low-dose mode.

RESULTS AND DISCUSSION

The first section of this chapter will deal with the aggregation of C8S3 molecules in a schematic fashion. Subsequent to that, experimental results will be presented and discussed as they were obtained from different experiments. Finally, bundles of single aggregates as a second thermodynamically stable configuration will be addressed in detail in the last section.

4.1 AGGREGATES OF C8S3

A closer look on the chemical structure of C8S3 (cf. figure 8) reveals that the molecule can be decomposed into three subgroups, i.e. hydrophobic octyl groups (depicted in red), hydrophilic sulfopropyl groups (depicted in blue) and the chromophore with an extended π -electron system (depicted in grey).

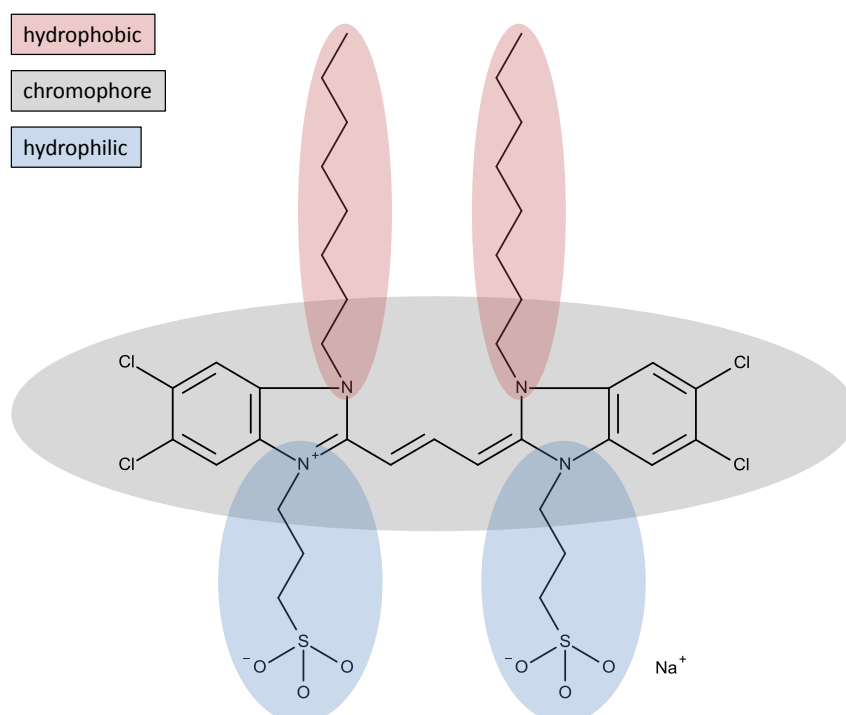


Figure 9: Chemical structure of C8S3 with its side groups highlighted by their interaction with the environment.

Upon dissolving C8S3 in methanol, which interacts with both hydrophilic as well as hydrophobic side groups, no aggregation occurs, because no driving force for that process is provided. Adding water to the C8S3/methanol solution, however, initiates aggregation as soon as the methanol content drops below a certain threshold concentration. By titrating methanol into a direct route sample solution (initial dye concentration: $5.75 \times 10^{-5} \text{ mol l}^{-1}$) and recording absorption spectra at each step, von Berlepsch *et al.* reported that for a methanol content exceeding 34 vol % no traces of aggregation could be found.[38] Obviously, water molecules have strong interactions with the hydrophilic side groups of C8S3 and, as a consequence, the system tries to minimize its Gibbs free energy by forming aggregates, where the hydrophobic side groups are screened from water and only interact with each other via van der Waals forces. This gives rise to a double-walled tubular structure consisting of two telescoped cylinders, as depicted in the figure below.

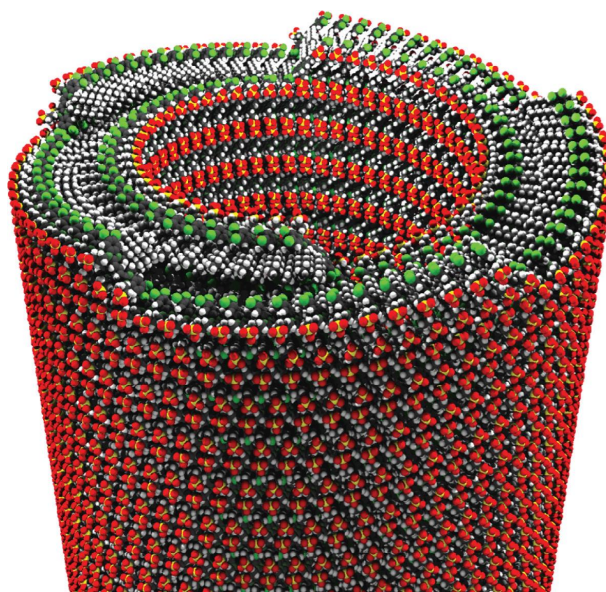


Figure 10: Illustration of a double-walled cylindrical aggregate of C8S3. Here red/yellow parts are hydrophilic, green/black parts represent the chromophores and white chains depict the hydrophobic side chains. Figure taken from [13].

In the following sections experimental results on C8S3 aggregates from various techniques will be presented to test the proposed structure.

4.2 ABSORPTION SPECTRA

4.2.1 Linear Absorption Spectra

Two representative linear absorption spectra for an alcoholic route as well as a direct route sample solution are depicted in the figure 11. Both are compared to the monomer spectrum for C8S3 dissolved in methanol, respectively. To ensure comparability of all spectra, the extinction ϵ , which also accounts for the concentration of the respective sample solution, is plotted instead of optical density.

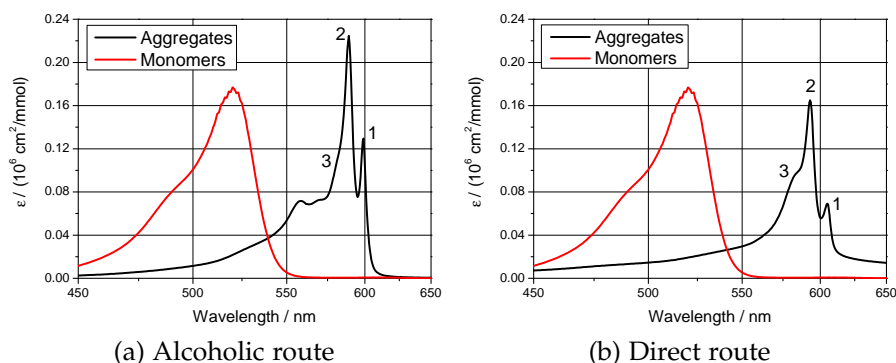


Figure 11: Absorption spectra of both alcoholic route and direct route sample solutions.

As obvious from figure 11a, the aggregate spectrum in the alcoholic case features two strong peaks at 599 nm and 589 nm (also referred to as band 1 and 2), a shoulder at approximately 580 nm (band 3), two additional weak peaks at 570 nm and 558 nm and a very slight bump at 525 nm. In contrast, the direct route spectrum only shows three distinct features, i.e. two peaks at 603 nm and 593 nm (again band 1 and 2) and a shoulder at 584 nm (band 3). All these values coincide well with values reported earlier in literature.[39, 40, 41]

The notable features of the aggregate spectrum in comparison to the monomer spectrum are (i) the strong redshift in absorption by about $\Delta\lambda = 60$ nm (equivalent to 1980 cm^{-1}) in both cases, which can readily be observed by bare eye (cf. appendix, figure 32), (ii) the evolution of distinct peaks and (iii) the narrowing of linewidths of the respective peaks. The origin of (i) and (iii) goes back to the theory of J-aggregates as presented in sections 2.3.1 and 2.4. However, to explain the several dom-

inant peaks in the absorption spectrum one needs to consider the aggregate morphology.

The double-wall structure as introduced in the previous section strongly suggests that spectral features can be assigned to the inner and outer cylinder. As a first step to associate spectra and morphology, polarization sensitive absorption measurements were done by a number of other groups, where C8S3 aggregates were aligned by pumping the sample solution through a very thin cuvette and illuminating them with light polarized either parallel or perpendicular to the flow direction. These measurements have shown that band 1 and 2 have a transition dipole moment oriented parallel to the aggregate axis, whereas band 3 has a transition dipole moment oriented perpendicular to that and is either 2-fold degenerate or could not be detected due to the limited spectral resolution.[29, 39, 42] The transition dipole moments are illustrated in the figure below.

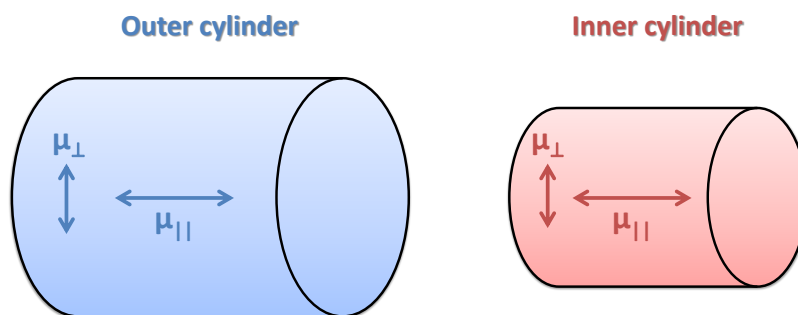


Figure 12: Transition dipole moments of inner and outer cylinder giving rise to multiple transition as observed in the absorption spectrum.

Features at 570 nm, 558 nm and 525 nm did not show any polarization dependence, but absorbed isotropically.[41] An exemplary spectrum is shown in the appendix (cf. figure 33).

Additionally, using variations of the environment in form of changing the composition of the solvent or introducing surface active additives like silver nitrate (AgNO_3), for instance, the absorption of band 2 could be strongly quenched, while band 1 remained more or less unaltered. [43, 44] That means band 2 arises from the outer cylinder and band 1 from the inner, as the outer cylinder's contact area with the solvent is much larger and therefore its optical properties are much more susceptible to changes in the environment.

By comparing alcoholic and direct route spectra in figure 11 one immediately sees that the peak height as well as the peak height ratio are different. Furthermore, while the extinction coefficient in the alcoholic route spectrum goes nicely to zero for wavelengths greater than roughly 625 nm, there is still a substantial degree of absorption in that spectral region in the direct route case. The same also holds for the blue side of the spectrum, i.e. in the proximity of 450 nm. This observation is easily explainable by the fact that C8S3 is hardly solvable in water. As a consequence, part of the small C8S3 grains did not dissolve completely within 24 h despite stirring and therefore resided in the solution as tiny particles contributing to scattering. This was also observable by bare eye, as the direct route sample solution were generally slightly more opaque than its alcoholic route counterparts. To some extent this effect also explains the reduced peak height of the direct route sample solution. In fact, both sample solutions were prepared with (in good approximation) the same amount of C8S3, but due to the low solubility in the direct route case the real concentration is somewhat lower leading to a reduced optical density and consequently to a lower extinction.

Nevertheless, the exact mechanisms how methanol affects the morphology of C8S3 aggregates and accordingly the spectral response is yet to be explained in detail. Using cryoTEM, Kirstein and Daehne found that the alcoholic preparation route yields thicker aggregates (outer diameter 16 nm) compared to the direct route (outer diameter 13 nm), while the wall thickness of about 4 nm was conserved.^[40] One possible explanation might be the incorporation of methanol molecules into the aggregate structure, which causes the increased curvature. However, this requires further investigations. The impact of methanol on the morphology of C8S3 aggregates will be addressed in greater detail in section 4.5.1.

All in all, the spectral features of the C8S3 aggregates' absorption were in nice agreement with, on the one hand, predictions by theoretical J-aggregate models and, on the other hand, the proposed double-walled structure.

4.2.2 Stability of Aggregates

The stability of the aggregates was tested by recording a sequence of absorption spectra in intervals of 24 hours after preparation of an alcoholic sample solution. Between measurements the sample solution was stored at room temperature in the dark to avoid light exposure. Each time a fused silica cuvette (thickness 1 mm) with sample solution was freshly prepared and spectra were recorded within 10 minutes afterwards. The following graph depicts all absorption spectra taken over the course of 10 days.

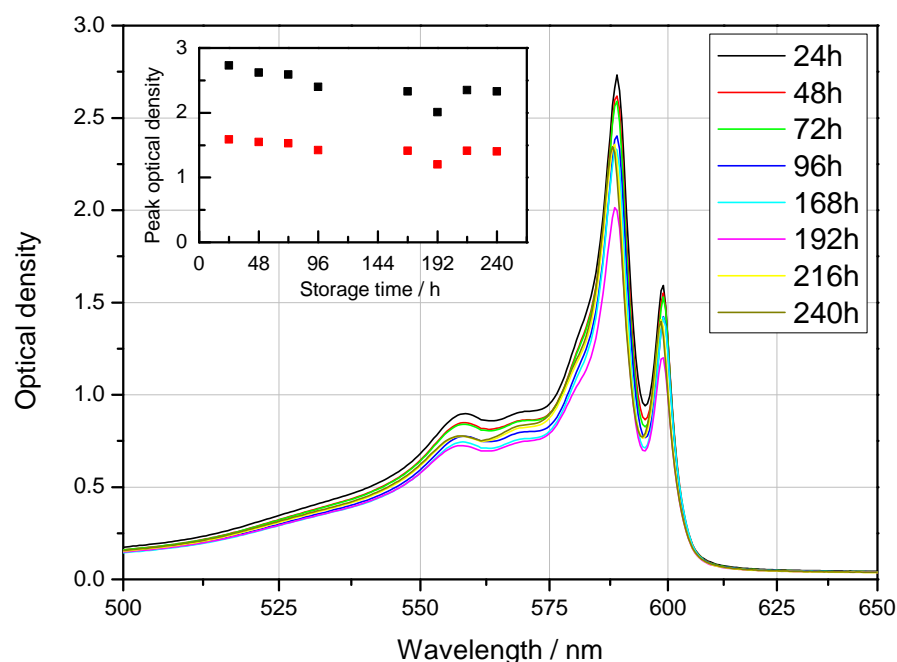


Figure 13: Sequence of absorption spectra over a duration of 10 days. The inset shows the evolution of the 589 nm peak (black) and the 599 nm peak (red) over time.

The inset in figure 13 shows the evolution of band 1 (red) and band 2 (black). While the high energy peak's optical density decreases from 2.73 to 2.33 (15%) within 10 days, the low energy peak's optical density undergoes approximately the same decrease of 12% from 1.59 to 1.40 in the same time. Besides, no additional spectral changes could be observed in the investigated time span, meaning none of the peaks shifted towards higher or lower wavelengths and no additional features evolved.

Of course, the decrease in optical density could arise from aggregates decaying into their monomeric constituents. However, in that case one would expect the signature of C8S3 monomers

around 525 nm to increase. As this is evidently not the case, one can conclude that the slight decrease in optical density is not related to the decay of C8S3 aggregates. Instead, aggregates tend to form bundles over time and eventually precipitate (cf. appendix, figure 38). As a consequence, the concentration of C8S3 aggregates drops over time reducing the overall optical density without rising the monomer signature.

To conclude, as long as sample solutions are stored avoiding light exposure, aggregates are stable over the course of days and weeks up to even months in exceptional cases (data not shown). However, aggregates might form bundles over time indicating that this is the thermodynamically more stable configuration (cf. section 4.6).

4.2.3 *Temperature-dependent Absorption Spectra*

Since the formation of C8S3 aggregates is a self-assembly process, the resulting structure is strongly dependent on environmental parameters, such as temperature, solvent, dye concentration, etc. In order to understand the role of temperature during the aggregation process and get further insights into assembly dynamics, temperature-dependent absorption spectra were recorded. Prior to the actual sample preparation all necessary ingredients, i.e. pure water and the stock solution (cf. section 3.2) were cooled/heated to the desired temperature of approximately 8 °C and 50 °C, respectively. Sample solutions were then prepared as usually and left for aggregation at the mentioned temperature for 24 h. Finally, they were filled into cuvettes and transferred to the absorption spectrometer. There, a sequence of 25 absorption measurements in steps of 1 minute was recorded. After that time the sample solutions were assumed to have reached room temperature. A selection of the recorded spectra is presented in the two graphs on the next page.

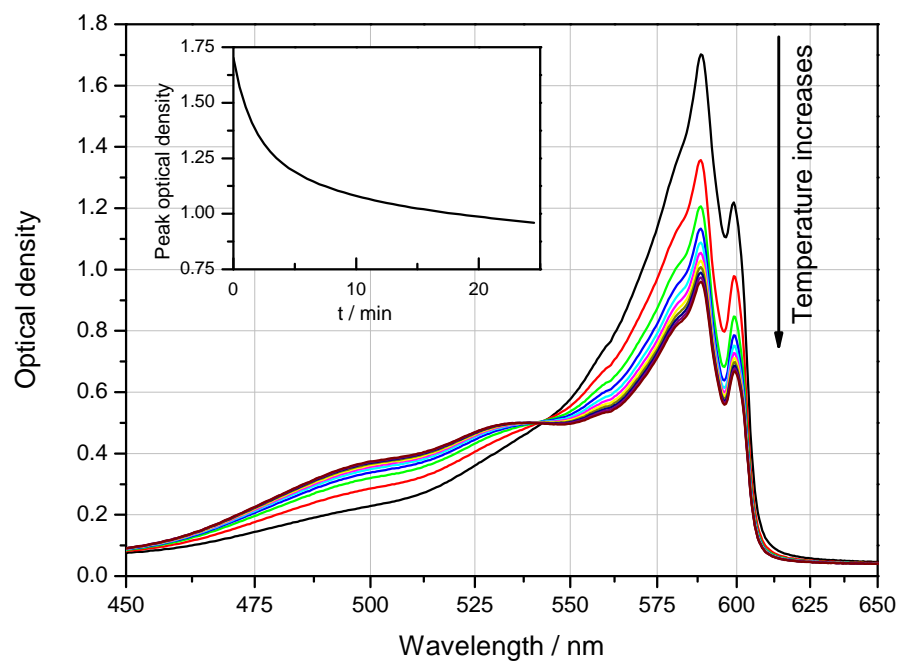


Figure 14: Sequence of absorption spectra for a cold (~8 °C) sample solution. The inset shows the evolution of the 590 nm peak height over time.

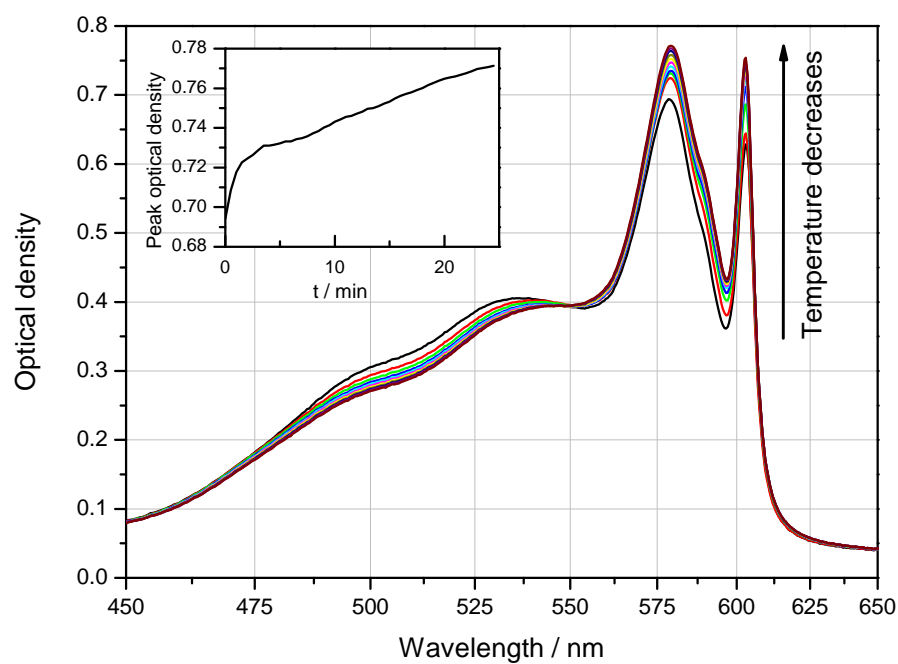


Figure 15: Sequence of absorption spectra for a hot (~50 °C) sample solution. The inset shows the evolution of the 579 nm peak height over time.

Starting with the discussion of the cold sample, the peak optical density of band 1 shows a significant decrease, as the temperature of the sample solution rises from $\sim 8^\circ\text{C}$ to room temperature (cf. inset of figure 14). The same trend also holds for band 2, which is not separately shown. At the same time, the spectra display an increase by roughly 0.2 in optical density around 500 nm. However, spectral shifts of features were not observed. Instead, all recorded spectra in figure 14 nicely resemble the alcoholic route spectra as expected (cf. section 4.2.1), with strong peaks at 599 nm and 589 nm and a shoulder at 580 nm. Admittedly, the shoulder is more distinct than in figure 11a masking the 570 nm and 558 nm features.

Assuming that the spectral signature around 520 nm originates from unaggregated monomers, the observed behaviour can be explained by C8S3 molecules being expelled from the aggregate structure as temperature goes up and hence increasing the optical density in the mentioned region. Logically, the optical density of band 1 and 2 decreases simultaneously, as the aggregates shrink in size and possibly in number.

In contrast to the cold sample, the spectrum of the hot sample solution did not show any strong trends upon cooling down from $\sim 50^\circ\text{C}$ to room temperature. Next to the increase of the peak optical density of band 1 from 0.62 to 0.75, a slight decrease in optical density in the spectral region around 520 nm could be observed. Here, the same reasoning as in the previous paragraph concerning the monomer signature can be applied. The initially elevated temperature causes C8S3 molecules to not be embedded in the aggregate structure, but as time proceeds and temperature drops those molecules are incorporated into the aggregates and, thus, rise the height of the two large peaks. However, it is not the trend upon cooling that is remarkable here, but the spectral shape itself. In fact, the spectrum does not resemble an alcoholic sample solution (cf. figure 11a) any longer. Instead, band 1 is shifted to 603 nm, band 2 is shifted to 591 nm and, furthermore, masked by an entirely new peak at 579 nm. Disregarding the latter, the obtained spectra are comparable to direct route samples, as presented in figure 11b. Apparently, the high temperature caused the evaporation of methanol (boiling point 65°C), although the flask containing the sample solution was sealed. As methanol was removed as an additional solvent, the spectrum was "switched" to direct route version. Such switching between alcoholic and direct route spectra has been shown before by von Berlepsch *et al.* via

titration of methanol to a direct route sample solution.[39] This experiment has shown that the process also works in the opposite direction. The significant change of the spectrum must arise from a change in morphology of the formed aggregates. Again skipping details at this point and referencing to section 4.6, a plausible explanation is the formation of bundles of aggregates. Here, thermal energy might be a factor that favours the formation of bundles. Besides, it is also possible that water evaporated to some extent leading to a higher concentration of C8S3, which again increases the likeliness of bundles to occur.

4.3 FLUORESCENCE EMISSION SPECTRA

4.3.1 *Monomers*

For the sake of completeness the absorption spectrum (in black) and the fluorescence spectrum (in red) of monomeric C8S3 dissolved in methanol are shown in the figure below.

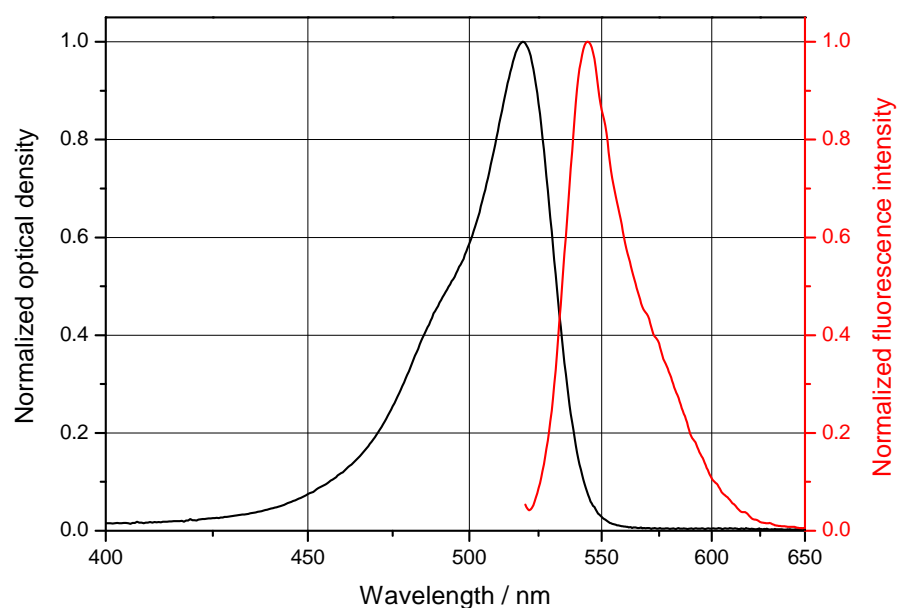


Figure 16: Absorption and fluorescence emission spectra of monomeric C8S3 dissolved in methanol. The latter was recorded after excitation at 510 nm.

The peaks of both curves are separated by a Stokes shift of approximately 24 nm that arises from fast internal relaxation of vibrational excited states and solvent reorganization before the electronic relaxation under emission of a photon occurs. A signature in fluorescence spectra in the spectral region around

550 nm will be likely due to non-aggregated C8S3 molecules, as already discussed in [29].

4.3.2 Aggregates

For both alcoholic and direct route sample solutions, the fluorescence emission spectra as obtained after excitation at 560 nm are plotted in figure 17. In order to make Stoke shifts recognizable, absorption spectra of both different routes were added. Last but not least, comparability of absorption and fluorescence spectra was ensured by respectively normalizing them to their peak values. The absolute peak height has no importance for the following discussion.

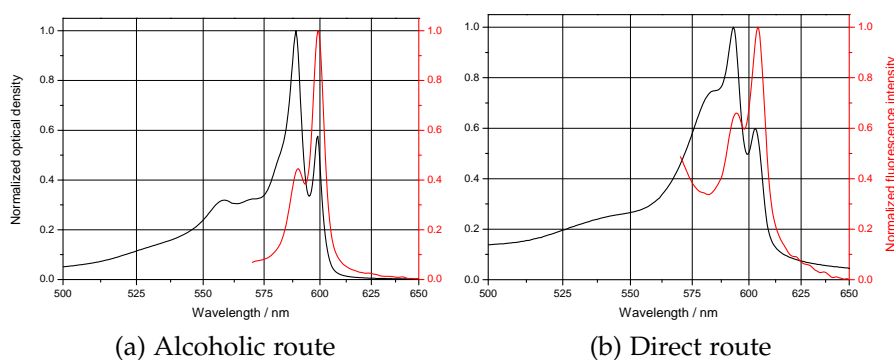


Figure 17: Fluorescence emission spectra in comparison to the respective absorption spectrum for both preparation routes.

As apparent from figure 17, the peak positions of emission and absorption coincide in both cases, meaning that independent of preparation route, a Stokes shift is almost absent. In fact, only a slight shift of the fluorescence signal of approximately 1 nm towards higher wavelengths was found. Furthermore, none of the high energy features (between 500 nm and 580 nm) that were addressed in section 4.2 showed a signature in fluorescence. Also decreasing the excitation wavelength and therefore increasing the excitation energy did not reveal any distinct features (cf. appendix, figure 34). Additionally, the peak height ratio of band 1 and 2 in both fluorescence spectra is reversed compared to the absorption spectra, meaning that the bulk of emitted photons arises from the low energy transition (~ 600 nm) and only a small share originates from the high energy transition at ~ 590 nm. As a matter of fact, the latter signature was not detectable for non-diluted sample solutions, be-

cause of reabsorption of emitted photons contributing to the low energy transition afterwards.

For the direct route sample solution (cf. figure 17b), the increase in fluorescence intensity when approaching the excitation wavelength can be explained by scattering. As discussed earlier in section 4.2.1, small particles of undissolved C8S3 reside in the solution. Therefore, incident excitation photons might be scattered towards the detector and falsely contribute to the fluorescence signal. Accordingly, this behaviour was not observed in the alcoholic route case.

Before starting with the discussion, it is important to note that both fluorescence bands are formed after intraband relaxation, as the transition following excitation at 560 nm is not related to a particular tubule, as evident from the LD spectrum discussed in section 4.2.1. Instead, high-lying states are populated first and subsequent fast relaxation leads to the population of the optically dominant states in the exciton bands.[29].

The probably most intriguing information to be extracted from the fluorescence spectra is related to the reversed peak height ratio. The fact that band 2 absorbs almost twice as many photons as band 1, but at the same time emits significantly less than band 1 is a strong indication for coupling between the cylinders. If the cylinders were completely uncoupled, the fluorescence intensity would simply reflect the number of molecules in one cylinders, as the fluorescence signal scales with the number of luminescing sites. In that case one would either expect both peaks having approximately the same height or band 2 exhibiting a stronger fluorescence signal due to the increased size and stronger absorption. Evidently, the opposite is the case, which immediately suggests efficient energy transfer from the outer to the inner wall. Further evidence for this hypothesis was provided by Pugžlys *et al.*, as they investigated the fluorescence of C8S3 at 5 K and found that for low temperatures the fluorescence signal of band 2 is strongly quenched compared to band 1, but still detectable.[45] Assuming a similar energetic structure of inner and outer cylinder, one would expect the peak height ration of band 1 and 2 be rather unaffected by a change in temperature for uncoupled cylinders, because the aggregate size does not changed over decreasing the temperature.

The second conclusion to be drawn from fluorescence spectra is the absent Stokes shift. As explained in the previous subsection, a Stokes shift arises from solvent reorganization and internal vibrational relaxation after a vibronic transition, which lead

to a loss of energy in form of heat. As this loss is apparently not present in C8S3 aggregates, the energy states involved in the transitions of band 1 and 2 are located at the bottom of an exciton manifold. According to the Franck-Condon principle, the transition from the vibrational ground states of both exciton manifolds to the ground state is therefore most likely.[26]

In summary, the shape of the fluorescence spectra clearly indicated that inner and outer wall of C8S3 aggregates are electronically coupled and efficient energy transfer occurs. Though, steady-state spectra could not elucidate the energy transfer dynamics between the two walls and therefore more elaborate experiments are required. Furthermore, the absence of a Stokes shift provided a first hint for the electronic structure of C8S3 aggregates.

4.4 TIME-RESOLVED FLUORESCENCE SPECTRA

The raw data as obtained during measurements at the fastest timebase is shown in the figure below (cf. section 3.3.3 for experimental details). Here, the vertical axis depicts wavelength in nm and the horizontal axis time in ps.

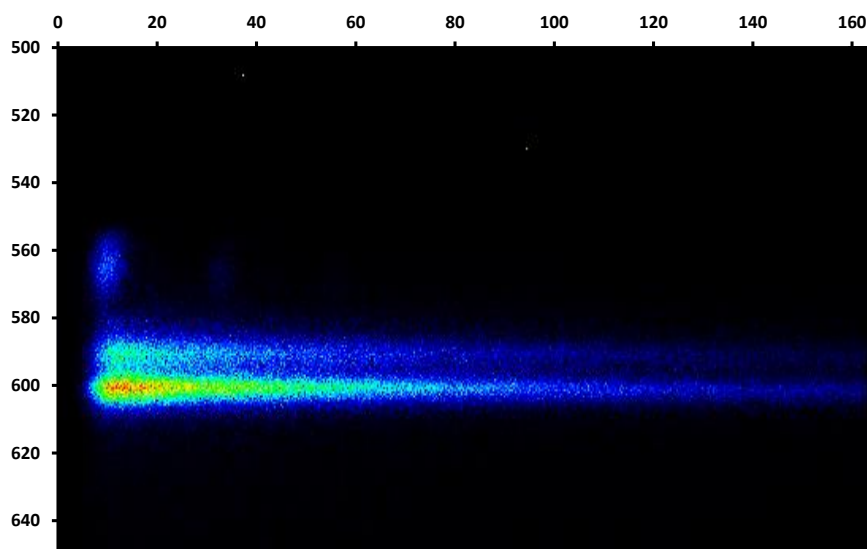


Figure 18: Raw data of time resolved fluorescence measurements.

The two fluorescence bands around 600 nm (band 1) and 590 nm (band 2) are clearly visible, as expected from static fluorescence spectra (cf. section 4.3). Besides, the scattered excitation light that leaked through the cut-off filter as explained in

the experimental section 3.3.3, is seen at approximately 560 nm. The temporal FWHM of that excitation pulse is equal to 5.2 ps and since the actual pulse length is much shorter than that, namely 120 fs (disregarding dispersive effects), this value can be used as the time resolution of the system. Lastly, after approximately 30 ps there is a very weak signal at 560 nm, which due to the reflection of the excitation pulse at the backside of the cuvette. Simply calculating $\Delta x = c \times \Delta t = 30 \times 10^{-12} \text{ s} \times 3 \times 10^8 \text{ m/s} = 9 \text{ nm}$ and accounting for setup geometry and refractive indices justifies this explanation.

By integrating along the time axis of the raw data one obtains the spectrally resolved signal (cf. figure 19), which nicely resembles the fluorescence spectra as presented in figure 17 in the previous section. In fact, this finding proved that the sample was in good order and one could proceed with the further evaluation.

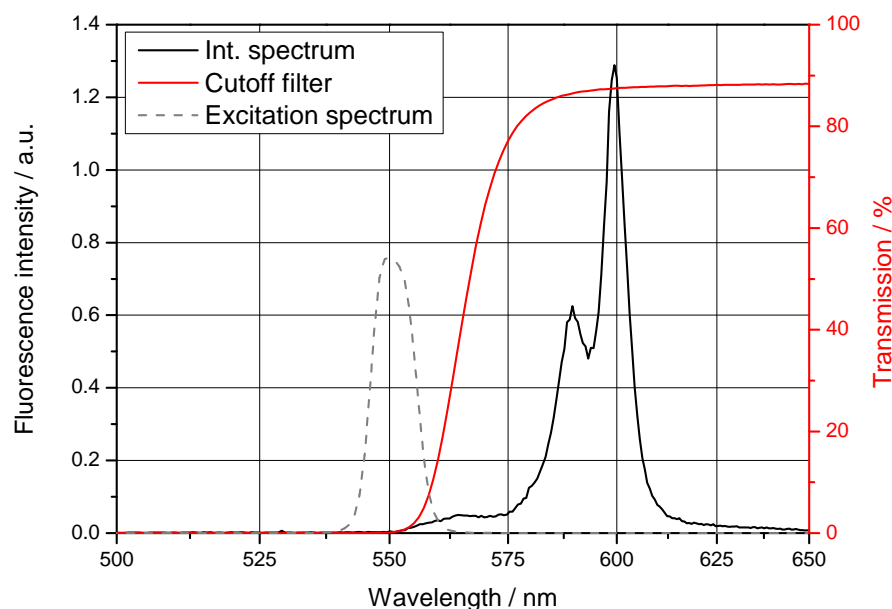


Figure 19: Spectrum as obtained via integration along the time axis. The transmission spectra of the used 560 nm cut-off filter and the 550 nm bandpass filter are added in red solid and red dotted line, respectively.

In figure 18 one notices that the fastest timebase with a maximum time window of roughly 160 ps is not sufficient to capture the whole fluorescence decay of C8S3 aggregates. In order to display the slowly decaying components of the fluorescence signal as well, the experiment was also performed at the slowest timebase with a time window up to 1.5 ns, but with a

worse resolution. The transients, that are depicted in the figure 20, were obtained by spectrally integrating the raw data over a small area around the bands at 590 nm and 600 nm, respectively. Note that in the following discussion time zero will be set as the moment of excitation, hence, coinciding with the peak of the laser pulse.

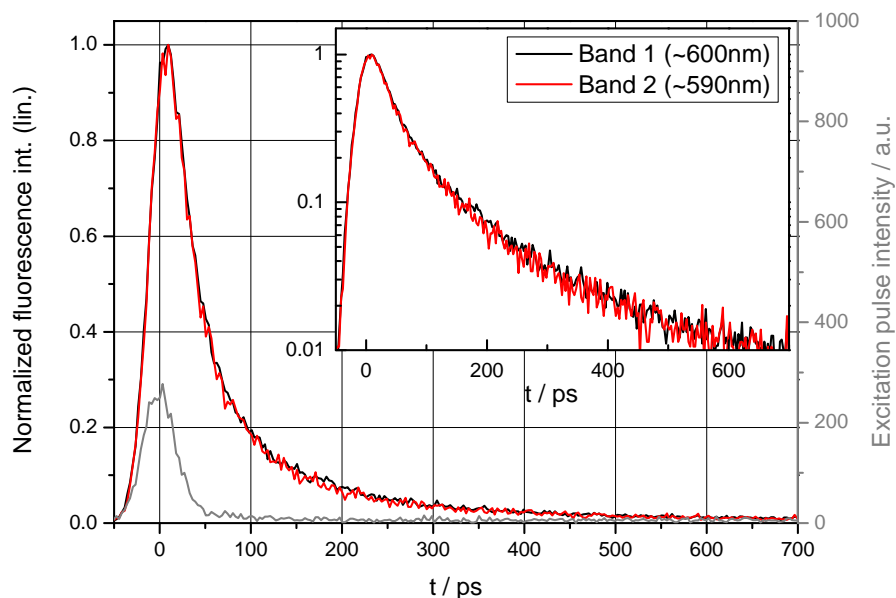


Figure 20: Normalized transient of the fluorescence signal as measured with a slow timebase to also capture photons emitted after up to 700 ps after excitation. The inset shows the same data plotted with logarithmic scaling. Also the after-pulse as previously discussed is distinctively recognizable.

Obviously, band 1 and 2 show an identical fluorescence intensity decay over time. The logarithmic plot in the inset proves that both decays are non-exponential, which is in line with findings for low temperatures reported by Pugžlys *et al.*[45] Otherwise, one would expect a straight line here. Moreover, both graphs also have the same rise time, as evident from the coinciding peak positions in figure 20. The peaks are situated at approximately 10 ps after the laser pulse reaches its peak, as depicted in grey. This is close to the temporal resolution of the system and, therefore, it cannot be used to draw any reliable conclusions. Last but not least, the transients do not exactly approach zero intensity meaning that there is some background signal resulting in a baseline, which will become important for the fitting routine later.

For an enhanced time resolution, figure 21 depicts the normalized fluorescence transients of band 1 and 2 recorded for the fastest timebase. One notices that the non-exponential decay is not distinctively recognizable from the logarithmic plot in the inset. However, it turns out that the non-exponential decay is masked by noise, which is undeniably more present in the fast timebase case. Responsible for that is the shorter capture time for fast timebase measurements, as in this mode the setup is more susceptible to temporal shifts during data acquisition. In fact, drawing straight lines through the initial decay part and the tail of the logarithmic fast timebase graph proves a non-exponential decay behaviour.

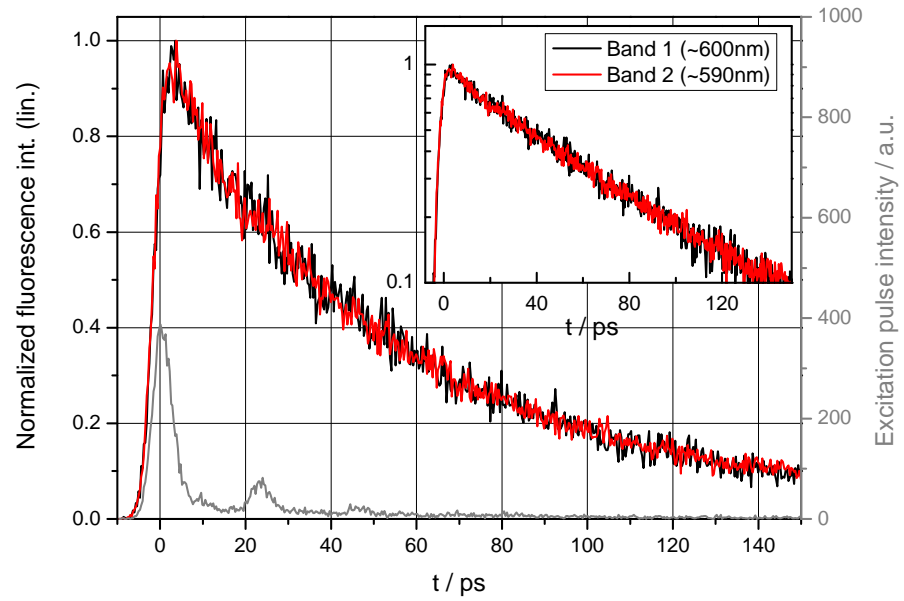


Figure 21: Normalized transient of the fluorescence signal as measured with the fastest timebase. The inset shows the same data plotted with logarithmic scaling.

Due to the non-exponential decay the presented transients can not be fitted with a simple single exponential decay constant. Instead, one has to assume a convolution of a Gaussian function and a number N of exponential functions with decay constants τ_i . The exact expression is rather technical and thus mentioned in the appendix (cf. equation 10).

For the fast timebase (ft) a decent fit could be achieved by assuming two decay constants (τ_1^{ft} and τ_2^{ft}), which is obviously the minimum number of exponents for a non-exponential decay as observed. In contrast, the transient in figure 20 for the slow timebase (st) could not be fitted using only τ_1^{st} and τ_2^{st} ,

but a third decay constant τ_3^{st} was required to account for the slowly decaying components. Assuming that the rapidly decaying components are equal, τ_1^{ff} and τ_2^{ff} could be used as initial values for τ_1^{st} and τ_2^{st} . An additional fitting parameter for the baseline was necessary to obtain a good match between data and fit. The results of both fitting routines are summarized in the table below.

	τ_1 / ps	τ_2 / ps	τ_3 / ps	tc / ps
Fast timebase	13 ± 3	66 ± 1	-	54 ± 5
Slow timebase	17 ± 2	58 ± 6	219 ± 21	57 ± 5

Table 1: Summary of decay constants τ_i as obtained from the fitting routine on the two different data sets including the standard deviation. For the following discussion also the time constant (tc) defined as the time at which the transient decays to $1/e \approx 0.37$ of its peak value, was added. Here, the error refers to the resolution of the system.

The first conclusion that can be drawn is connected to the sheer number of decay exponents. In fact, these imply that population relaxation in C8S3 aggregates has multiple possible pathways, which underlines how sophisticated energy transport and transfer in the system actually is.

Unfortunately, there is barely data available in literature for time-resolved fluorescence experiments that could serve for comparison of these figures, especially not for ambient conditions. Pugžlys *et al.* investigated the fluorescence evolution of C8S3 aggregates (prepared via the direct route) at low temperatures and found a significant difference in decay dynamics for band 1 (inner cylinder) and 2 (outer cylinder).[45] At least for band 1 the decay time constant was in the same range as reported here, whereas for band 2 their data displayed a decay that was roughly twice as fast. As the fluorescence spectrum was more or less independent of the preparation route (cf. section 4.3), the observed mismatch is unlikely to be explained by that. As a logical consequence, the altered decay dynamics of band 2 must arise from the elevated temperature that leads to drastically different excited state population kinetics. Nevertheless, the exact mechanism remains an open question.

In the previous section it was argued that the fluorescence intensity ratio of band 1 and 2 indicates efficient energy transfer from the outer to the inner cylinder. In terms of time-resolved fluorescence measurements one could therefore expect a slower

decay or a delayed formation of band 2 meaning that the respective transient either reaches its peak later than band 1 or has a significantly longer tail, because excited state population needs to be transferred from one cylinder to the other. However, it is important to realize that band 2 is of course formed immediately after excitation, but the population transfer from band 1 to band 2 competes with the radiative fluorescence decay leading to altered transient. Note that for this process to be detectable in these measurements, the characteristic time constant needs to be in the range of a few ps. Evidently, this was not possible to observe with the given time resolution. However, one could indeed observe that the intensity ratio was in favour of band 1 right from the beginning of the measurement, meaning that the intercylinder energy transfer must occur on time scales that are beyond the time resolution of this system.

Augulis *et al.* used pump-probe experiments to exclusively excite the outer cylinder and observe the population formation on the inner cylinder by probing photobleaching, stimulated emission and photoinduced absorption over a broad spectral bandwidth. They reported that the formation of band 2 occurs after approximately 2 ps subsequent to excitation.^[46]

4.5 CRYOTEM

In order to test the proposed double-wall structure of C8S3 aggregate, a simple, yet promising strategy is to record actual pictures of the specimen. During the past decades, cryoTEM has been established as a useful tool for research dealing with soft materials and is thus also suitable for C8S3 aggregates.

CryoTEM micrographs were recorded for sample solutions of two different concentrations, once for the standard concentration of $c = 2.40 \times 10^{-4} \text{ mol l}^{-1}$ as described in section 3.2 and once for a higher concentration of $c = 2.92 \times 10^{-3} \text{ mol l}^{-1}$ to observe a stronger degree of bundling. Two representative pictures for both measurements are shown in figure 22. Dark spots in the presented cryoTEM pictures indicate stronger phase contrast, which in turn is associated with the amount of material electrons have to pass through and thus become phase-shifted. This phase-shift is then translated by the TEM into a visible intensity contrast. Conversely, white spots mean weaker phase contrast and thus less material. TEM micrographs are always 2D projections of 3D objects, which is an important aspect to consider when evaluating TEM results. However, the exact image formation in TEMs is beyond the scope of this thesis and will therefore not be discussed in greater detail, but can be looked up in literature devoted to that particular topic.[47]

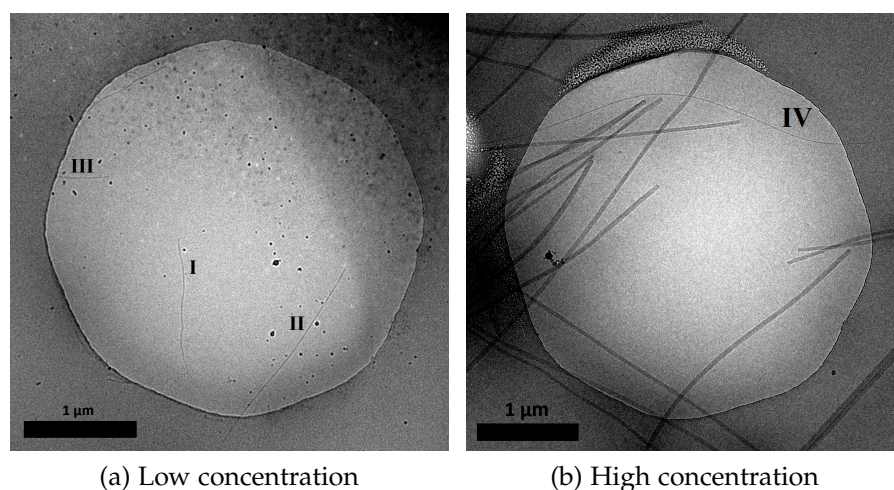


Figure 22: CryoTEM pictures recorded for two different sample solution concentrations at small magnification. The carbon grid that was used for the sample preparation is clearly visible. The contrast was adjusted slightly to make single aggregates recognizable.

For small magnifications of respectively 7800x (figure 22a) and 5000x (figure 22b) single aggregates are barely visible and therefore indicated by Roman numbers (I to IV). Obviously, the increased concentration of the sample solution affects the length of single aggregates as well as the degree of bundling (all thick structures). While in figure 22a the length of single strands is in the range of few μm , this value increases up to several μm as apparent from figure 22b.

To investigate the morphology of the aggregates as well as the bundles with special regards to the double-walled structure as suggested by absorption spectra (cf. section 4.2), cryo-TEM micrographs of higher magnifications are required. Two representative pictures of respectively 75 000x and 28 000x magnification are shown in the figure 23.

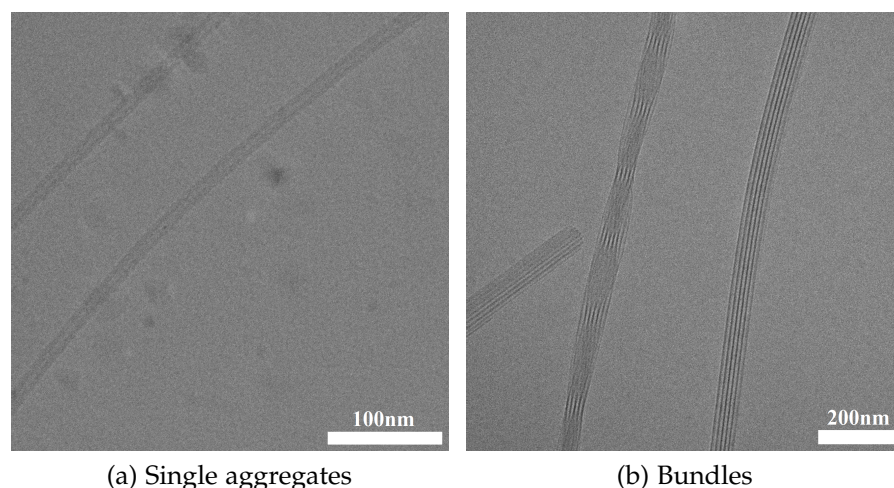


Figure 23: High resolution cryo-TEM micrographs of aggregates and bundles. Magnification: (a) 75 000x and (b) 28 000x.

The following two subsections will focus on the analysis of single aggregates and bundles of aggregates in cryoTEM micrographs separately.

4.5.1 *Single Aggregates*

Enlarging straight segments of the aggregates (see appendix, figure 36) and integrating along the tube axis resulted in precise line scans of the aggregate cross section. Figure 24 depicts such a segment with inner and outer walls highlighted in blue and red, respectively.

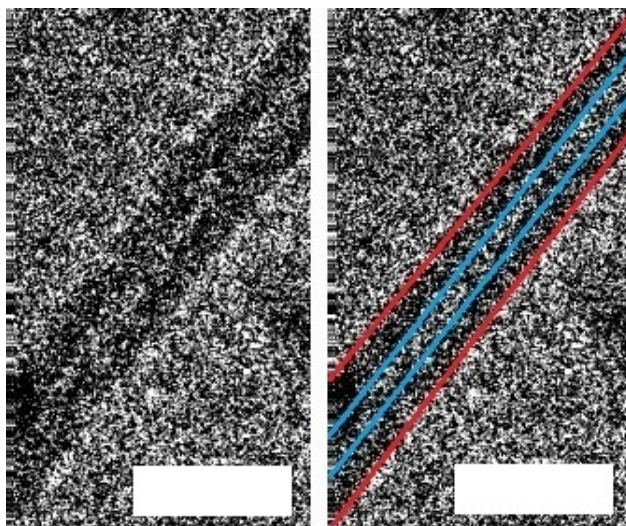


Figure 24: Single straight segment from an aggregate for further analysis. Red and blue lines highlight the outer and inner wall of the double-walled tube. White bar = 25 nm.

An exemplary single line scan is attached to the appendix, see figure 37. From these line scans the inner and outer diameter of a single aggregate could be determined. By repeating this for all segments the figure shown below was obtained.

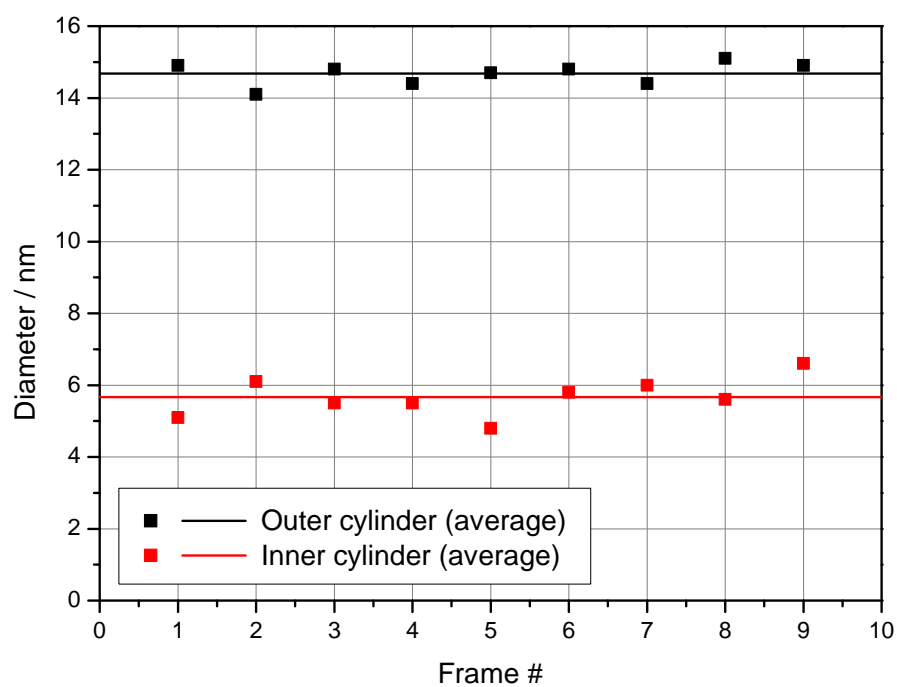


Figure 25: The measured inner and outer diameter of a single aggregate versus frame number.

The average outer and inner diameter displayed as solid lines in figure 25 are $\varnothing_{\text{outer}} = 14.7 \pm 0.3$ nm and $\varnothing_{\text{inner}} = 5.7 \pm 0.6$ nm, respectively. Hence, the wall thickness of one aggregate can be calculated to be $d_{\text{wall}} = 4.5 \pm 0.4$ nm. Recalling the size of one C8S3 molecule from section 3.1, one immediately notices that the wall thickness is in nice agreement with twice the size of one molecule, as measured from the end of the hydrophilic to the end of hydrophobic side chain. To test whether these values are consistent with literature values, table 2 summarizes diameters of C8S3 aggregates prepared via different routes as reported by several groups.

Author	Prep.	$\varnothing_{\text{outer}}$ / nm	$\varnothing_{\text{inner}}$ / nm	d_{wall} / nm	Ref.
Kirstein <i>et al.</i>	alc.	13.0 ± 0.5	-	-	[44]
Kirstein <i>et al.</i>	alc.	~ 13	~ 5	~ 4	[40]
	dir.	~ 16	~ 8	~ 4	
von Berlepsch <i>et al.</i>	alc.	13.0 ± 0.5	5.0 ± 0.5	4.0 ± 0.5	[39]
	dir.	17.0 ± 0.5	8.0 ± 0.5	4.0 ± 0.5	
von Berlepsch <i>et al.</i>	alc.	13.0	5.8	3.6	[35]
Eisele <i>et al.</i>	alc.	13.0 ± 1.0	6.0 ± 1.0	3.5 ± 1.0	[43]
Own experiments	alc.	14.7 ± 0.3	5.7 ± 0.6	4.5 ± 0.4	-

Table 2: Inner and outer diameter as well as wall thickness of C8S3 aggregates as found in literature in comparison with the values reported here. The values are distinguished by different preparation routes, i.e. alcoholic and direct.

As apparent from table 2, the direct preparation route generally yields thicker aggregates with diameters in the range of 16.0 nm to 17.0 nm compared to the alcoholic preparation route. Interestingly, the wall thickness is not affected meaning that the presence of methanol during aggregation has equal impact on the curvature of both inner and outer cylinder.

All in all, values obtained for this thesis agree well with those presented in literature. However, one notices that the value for $\varnothing_{\text{outer}}$ of 14.7 nm is situated in between the values reported for direct route samples (~ 13.0 nm) and alcoholic route samples (~ 17.0 nm). Taking a closer look at the exact preparation conditions, one finds that in all cases listed in the table the methanol content during aggregation was around 20 wt %. In contrast, the amount of methanol used for preparation here was by approximately factor 2 lower, i.e. around 10 wt %. This prompts the conclusion that the curvature of inner and outer cylinder of

C8S3 nanotubes scales with the methanol concentration during aggregation.

As the direct route preparation is one extreme case with an methanol content of 0 wt %, the respective curvature is lowest, which corresponds to the thickest diameter attainable. Increasing the methanol concentration leads to an increase in curvature and thus a decrease in thickness down to ~ 13.0 nm as reported. As mentioned in section 4.1, theoretically the methanol content can be raised up to 34 vol %, which translates to 29 wt %, before aggregation is completely inhibited. However, the question whether the curvature increases further for an even higher methanol content or saturates at some point remains open and requires additional investigations.

Coming back to figure 25, it is intriguing that none of the data points deviates strongly from the average value, meaning that the aggregate is nicely uniform throughout the entire length of approximately 600 nm that is depicted in figure 23a. This uniformity allows for calculating the average over all individual line scans, from which one obtains figure 26a.

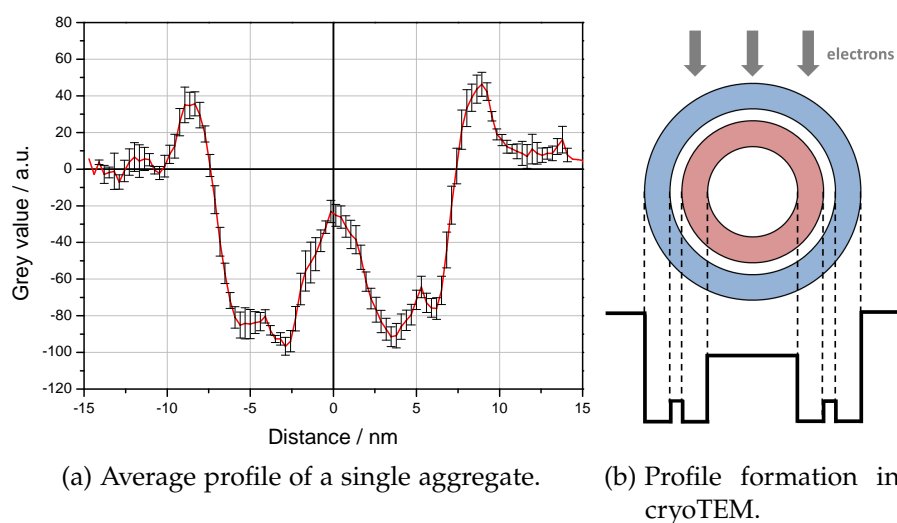


Figure 26: (a) average line scan as calculated from nine individual scans. The bars are indicating the standard error. (b) schematics of the profile formation in cryoTEM measurements. Blue colour depicts the outer and red colour the inner cylinder. As mentioned before, more material gives rise to stronger contrast and therefore a larger dip.

The double-wall structure is now evident from the large peak at zero position and the two small peaks at roughly -4.6 nm and 5 nm. It is remarkable that these small peaks became vis-

ible after averaging over nine individual scans, which underlines the uniformity and low degree of disorder in the aggregates. In the individual scans the mentioned peaks could not be distinctively identified (cf. appendix, figure 37). Figure 26b illustrates the relation of the line scan and the actual aggregate structure. Note that any interdigitation of hydrophobic chains is disregarded in that schematic figure.

Last but not least, the positive peaks at approximately -8 nm and 8 nm do not have a physical meaning regarding the aggregates, but are due to Fresnel fringes. In some of the cryoTEM pictures presented here or in literature this is observable as a white rim at the edge of aggregates or bundles (cf. figure 24, left side). Fresnel fringes are an interference effect that occurs for images of objects that are out of focus, which is usually the case for TEM micrographs. In fact, the latter are recorded for a certain defocus in order to enhance the phase contrast and related to that the spatial resolution. Further details can be looked up in specialized literature, such as [47].

As a closing remark of this section, first molecular dynamics (MD) simulations on C8S3 aggregates have been published recently by Megow *et al.*[48] There, a structure with fully interdigitated octyl chains (cf. figure 9) was proposed, which corresponds to a distance of 1.3 nm between the centres of the π -electron systems. Using simple geometrical considerations, one finds that the total thickness in this case amounts to roughly 2 nm, which is significantly smaller than the lowest experimentally found value of 3.5 nm.

4.5.2 Bundles

A second species observed in cryoTEM micrographs were bundles of single aggregates (cf. figure 23b). Accordingly, those structures are much thicker and easier to observe.

An intriguing feature of bundles is that they occur with different helicities. Figure 23b displays examples of bundles showing absolutely no twist (right side) and strong twist (left side). Nevertheless, the phenomenon of helical bundles is not subject of this thesis, but was intensively investigated elsewhere.[49, 50]

For studying the morphology of bundles, it is sufficient to focus on straight bundles only. In contrast to the previous case of single aggregates, the acquisition of accurate line scans for bundles of C8S3 aggregates was straightforward. As a matter of fact, it was not necessary to integrate along the tube axis due to

the sheer size of bundles. One exemplary line scan is depicted in the following figure.

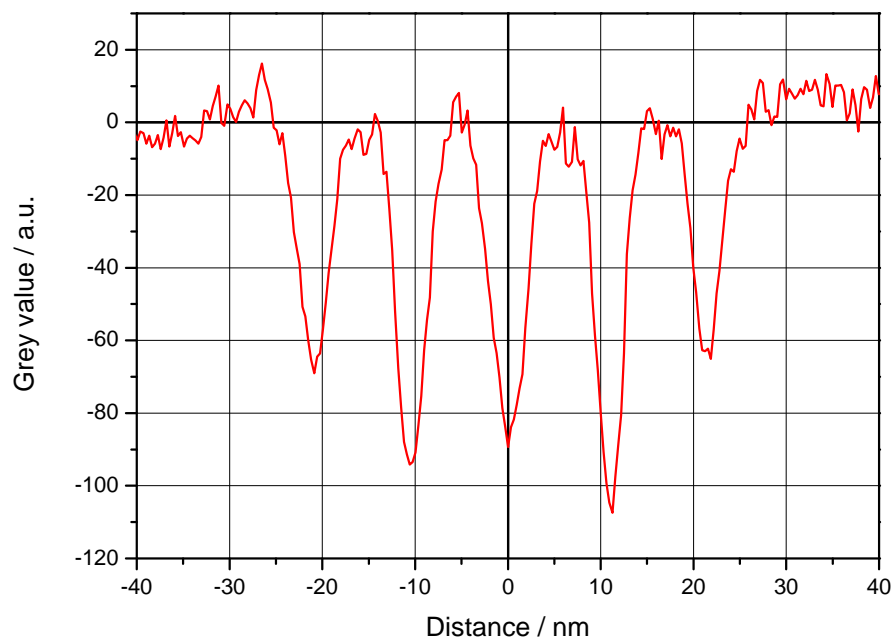


Figure 27: Line scan of a bundle of aggregates. The scan was obtained on a bundle, where helicity was absent.

As apparent from figure 27, the respective dips show a repetition distance that is equal to approximately 10.4 nm. In which manner this relates to the actual structure will be addressed in the next section.

4.6 BUNDLES OF C8S3

Bundles of single C8S3 aggregates have been mentioned in the previous sections as the thermodynamically most stable configuration of C8S3 in aqueous solution. Accordingly, bundling occurs automatically over time, as the system tries to minimize its Gibbs free energy. However, it can also be purposely induced by increasing the dye concentration, rising the temperature during the aggregation process or introducing some impurities to the system, for instance. The figure below depicts absorption spectra of a freshly prepared sample solution (black curve) in comparison to sample solutions, which were either stored for several months (red curve), annealed during the aggregation process (blue curve) or prepared with a high C8S3 concentration (green curve). Despite the latter all solutions were made

using the direct route. Therefore, it will be excluded from the following discussion and addressed in a separate paragraph.

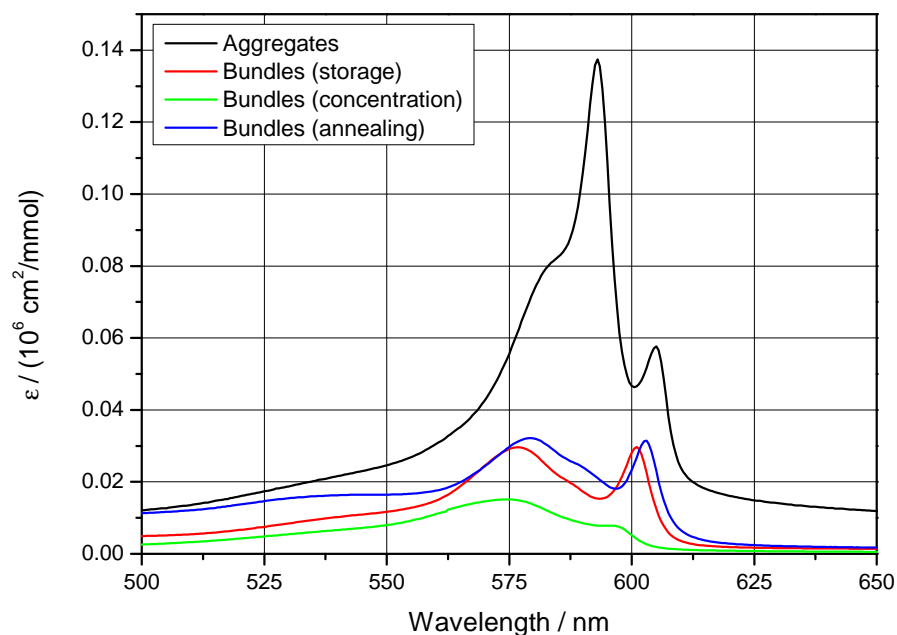


Figure 28: Absorption spectra of aggregates and bundles in comparison.

Disregarding the strong decrease in extinction for a moment, one notices that in good approximation the 603 nm transition (band 1) remains unaltered for the red, blue and black curve. It is astonishing that also the linewidth of the transition is preserved. Meanwhile, the 593 nm peak (band 2) is strongly quenched and only detectable as a weak shoulder in the red and blue spectra. Interestingly, in both cases a new feature at approximately 578 nm evolves with roughly the same peak height as band 1. The overall optical density is, however, reduced to a large extent compared to the single aggregate spectrum. Last but not least, the spectral region around 525 nm is slightly more distinct in the annealed case than for the other spectra being indicative for non aggregated C8S3 molecules. These findings are in line with results presented in literature.^[41, 51]

As mentioned before, the sample solution of the green curve was prepared via the alcoholic route. Thus, it is not surprising that the spectrum is shifted to the blue side, which is consistent with spectra recorded earlier (cf. section 4.2). Nevertheless, the overall trend, i.e. strong quenching of extinction and the evolution of a high energy peak in the vicinity of 575 nm also holds in this case.

Section 4.2.1 has proven that the shape of the spectrum and the morphology of the aggregates are directly related to each other. Using that, one can conclude that a morphological change goes hand in hand with the bundling process, as the optical response changes drastically. Intuitively, one would expect that bundles are formed by single aggregates that simply stick together. Yet, that would violate findings from cryoTEM, because compact stacking of aggregates as a whole engenders a repetition distance of dips of around 14.7 nm (outer diameter) in line scans. Evidently, this is not the case, but one finds 10.4 nm instead. By taking only the morphology into account, one could explain the latter finding by considering only inner cylinders forming bundles. The repetition distance of dips in this case would be equal to $d_{\text{wall}}/2 + \varnothing_{\text{inner}} + d_{\text{wall}}/2 = d_{\text{wall}} + \varnothing_{\text{inner}} = (4.5 \pm 0.4 \text{ nm}) + (5.7 \pm 0.6 \text{ nm}) = 10.2 \pm 1 \text{ nm}$, which is in amazing agreement with the actually found value. Furthermore, for this particular way of forming bundles the spectral signature of the outer cylinder (band 2) is expected to vanish, while the spectral position and linewidth of the inner cylinder signature (band 1) should be conserved. This is indeed the case, as obvious from the spectrum shown in figure 28, again neglecting the drop in extinction. Bundling of exclusively inner cylinders is schematically depicted in the figure below.

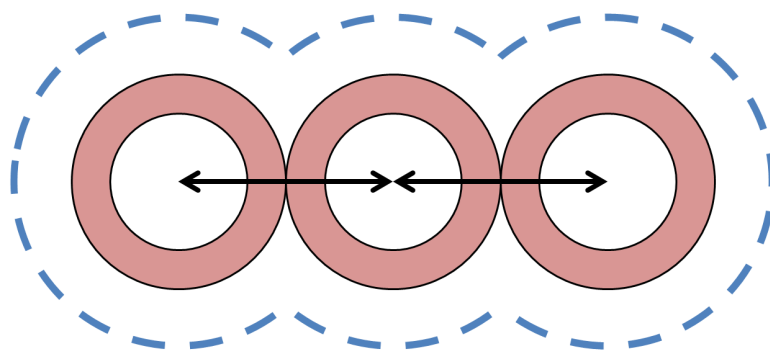


Figure 29: Red rings represent the inner cylinder, while the outer shell of such a bundle only schematically depicted by the blue, dotted lines. The black arrows have a length of 10 nm.

Due to the hydrophobic character of the octyl groups, it is very likely that the whole bundle structure is covered by a layer of aggregated C8S3 molecules, as indicated by the dotted, blue lines in figure 29. If this was not the case, these side groups

would be fully exposed to the aqueous solvent environment, which is highly unfavourable from an energetic point of view.

Now, one needs to explain the tremendous drop in extinction upon bundling. In fact, C8S3 bundles might eventually reach a physical size at which they precipitate from solution (see appendix, figure 38). Therefore, they are removed from the solution and do not contribute to absorption any longer. This explanation follows the argumentation as presented in the second last paragraph of subsection 4.2.2. Finally, the fact that spectral position and linewidth of band 1 remain equal, underlines the idea that the decline in optical density is due to precipitation and not due to formation of a different species.

Upon the formation of the proposed structures from single aggregates, at least part of the outer cylinder must be ripped off, because otherwise it would not be possible that only the inner cylinders stick together. Subsequently, there are two possible options for the expelled molecules: either they form new single aggregates or they reside in the solution as monomers. The slightly elevated optical density around 525 nm (cf. blue curve, figure 28) gives rise to the second hypothesis rather than to the first. Nevertheless, it can also be a mixture of both scenarios.

To conclude this section, bundling of single C8S3 aggregates is an interesting, yet (to date) unwanted side effect, because the formation of bundles is hard to control and cannot be excluded easily. However, by combining spectrum and cryoTEM data it was possible to unravel the structure of those bundles. Finally, it is noteworthy that highly sophisticated cryoET (cryogenic electron tomography), i.e. the 3-dimensional reconstruction of objects from cryoTEM micrographs, has been performed by different groups.[35, 41] All findings presented here are consistent with their results.

CONCLUSION AND OUTLOOK

The goal of this thesis consisted in investigating supramolecular self-assembled tubular aggregates of the amphiphilic cyanine dye C8S3 via cryoTEM and different spectroscopic techniques. Besides associating optical properties with the actual structure, understanding bundling of single aggregates as well as elucidating energy transfer processes were in the focus of interest.

CryoTEM images have shown the formation of double walled tubules upon dissolving C8S3 in pure water, with tubule lengths up to several μm and remarkably uniform inner and outer diameters of approximately 6 nm and 15 nm, respectively. Closely associated to this structure were the peculiar optical properties, which stem from the electronic coupling between single C8S3 molecules within the aggregate. As typical for J-aggregates, this coupling leads to a strong spectral redshift and the evolution of several narrow peaks, where most of the latter could be assigned to either the inner and outer cylinder of the double walled tubule. Furthermore, the aggregates' stability upon storage over weeks without any significant spectral and therefore morphological changes, could be taken as a second manifestation of the strength of intermolecular coupling. Nevertheless, bundles consisting of a number of single aggregates were observed as a second, but hitherto unwanted thermodynamically stable species, that occurred either upon very long storage, due to high dye concentration or a number of other factors.

Returning to the discussion of single C8S3 aggregates, fluorescence emission spectra exposed an interesting fact: the two main features of the absorption spectrum, i.e. two narrow peaks at roughly 590 nm and 600 nm, were also present in the fluorescence spectrum with an almost entirely absent Stokes shift, but a reversed intensity ratio. This observation is a clear indication for efficient intercylinder energy transfer, as proposed by Didraga *et al.*[29] In order to test this idea, time-resolved fluorescence measurements were carried out. Unfortunately, these could not reveal the mechanisms governing the energy transfer due to an insufficient time resolution. Hence, one can conclude that energy transfer in C8S3 aggregates must occur on a sub-ps time scale, which is in nice conformity with values

found by Milota *et al.* using 2D spectroscopy for aggregates of a similar cyanine dye derivative: C8O3.[52] A second question that remains open concerns the molecular packing within one aggregate. After averaging along the tube axis, the spatial resolution of cryoTEM images suffices to resolve the double walled structure, but lacks to resolve the molecular orientation. According to Würthner *et al.*, approaches to apply NMR spectroscopy for resolving the molecular packing have also failed so far.[10] Hence, a strategy to accomplish that has still to be developed.

The objective of this thesis was to catch up with the experimental progress on C8S3 aggregates in literature and obtain results that will serve as the foundation for further experiments. Especially the proper preparation of C8S3 aggregates turned out to be delicate due to the self-assembly process that is involved. In fact, one needs to ensure well defined conditions, as the sample preparation was very susceptible to environmental parameters, such as dye concentration, temperature, impurities in the solvent, etc. and already slight deviations lead to the formation of bundles or potentially other species. Although literature provides detailed descriptions of the actual sample preparation, it took a substantial amount of time to master it and obtain reproducible results. Having complete control of the system, however, is crucial for more advanced experimental techniques, such as 2D spectroscopy. The latter is a powerful tool that uses a sequence of ultrashort light pulses with variable delay to decipher the interplay of optical transitions, i.e. detect energy transfer channels.[16, 17]

Briefly, in 2D spectroscopy a sequence of four pulses is used to first excite the sample and subsequently measure the response of the system via heterodyne detection. Finally, Fourier transformation of the obtained data yields a two dimensional frequency map with the ω_{pump} and ω_{probe} on the x- and y-axis, respectively. While diagonal peaks ($\omega_{\text{pump}} = \omega_{\text{probe}}$) resemble the linear absorption spectrum, coupled transitions manifest themselves in off-diagonal peaks ($\omega_{\text{pump}} \neq \omega_{\text{probe}}$). Probing dynamics is possible due to an adjustable waiting time between the two excitation pulses.

Sperling *et al.* investigated exciton dynamics in C8S3 aggregates using 2D spectroscopy and found indeed proof for a common ground state of all excitonic bands as well as intertube exciton transfer.[53] However, not only intertube excitonic transport mechanisms are of interest, but also the intra-wall exciton

dynamics. In fact, using 2D spectroscopy two quantities will become accessible: the coupling of optical transition giving insights into the electronic structure of the underlying aggregate as well as the coherence (or incoherence) of excitonic motion. Understanding both is crucial for ultimately drawing conclusions about the intermolecular coupling and correspondingly molecular packing. Concerning the coherence of exciton dynamics, temperature dependent measurements are of special interest, as recently excitonic and vibrational coupling have been shown to play a role for the remarkable energy transfer properties.[54]

In brief, for a successful application of 2D spectroscopy, a sufficiently broad bandwidths of the pump and probe pulses is indispensable to simultaneously excite and probe all essential optical features of C8S3 aggregates, in this case. Absorption spectra have shown that this bandwidths should at least cover wavelengths from ~ 550 nm to ~ 610 nm or even broader in the ideal case. Building an optical parametric amplifier (OPA), which meets this requirement is one problem that needs to be (and currently is) tackled experimentally. As mentioned earlier, energy transfer mechanisms occur on a sub-ps, which is why ultrashort pulses are necessary to probe fast excitation energy dynamics. Using appropriate pulse compressors that compensate for dispersion effects, ultrashort pulses can be accomplished, while maintaining a broad bandwidths.[55, 56, 57]

APPENDIX

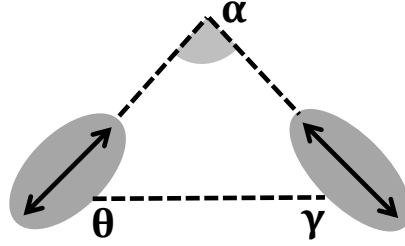


Figure 30: The mutual orientation of two (transition) dipole moments μ_1 and μ_2 separated by distance $|r_{12}|$ can be expressed in terms of angles α and θ . Here γ is an auxiliary angle, which will be helpful in the calculation beneath.

SIMPLIFICATION OF EQUATION 2

Starting point for the steps presented here is equation 2 as shown below.

$$V = \frac{(\mu_1 \cdot \mu_2)|r_{12}|^2 - 3(\mu_1 \cdot r_{12})(\mu_2 \cdot r_{12})}{|r_{12}|^5}$$

As a first step one has to write out the scalar products in terms of the angles α , θ and γ (cf. figure 30) as follows.

$$\begin{aligned}\mu_1 \cdot \mu_2 &= |\mu_1||\mu_2|\cos(\alpha) \\ \mu_1 \cdot r_{12} &= |\mu_1||r_{12}|\cos(\theta) \\ \mu_2 \cdot r_{12} &= |\mu_2||r_{12}|\cos(\gamma)\end{aligned}$$

By substituting these and the assumption $\mu_1 = \mu_2 = \mu$ into equation 2 one obtains:

$$V = \frac{|\mu|^2}{|r_{12}|^3}(\cos(\alpha) - 3\cos(\theta)\cos(\gamma))$$

Furthermore, one knows that $\alpha + \gamma + \theta = 180^\circ$. Combining this with the trigonometrical identity $\cos(x + \pi) = -\cos(x)$, one finally arrives at the expression mentioned in section 2.1 (cf. equation 3).

$$V = \frac{|\boldsymbol{\mu}|^2}{|r_{12}|^3} (\cos(\alpha) + 3 \cos(\theta) \cos(\theta + \alpha))$$

EXEMPLARY CALCULATION OF V

For in-phase, head-to-tail arranged dipole moments it is straight forward to see that $\boldsymbol{\mu}_1$ as well as $\boldsymbol{\mu}_2$ are parallel to r_{12} meaning that the scalar products in equation 2 become multiplications. Therefore, one can write down the following simplified equation.

$$V = -2 \frac{|\boldsymbol{\mu}|^2}{|r_{12}|^3} < 0$$

Since $|r_{12}|$ is a positive quantity, V is smaller than 0 in the above equation.

In the out-of-phase configurations $\boldsymbol{\mu}_1$ and $\boldsymbol{\mu}_2$ and antiparallel, which translates into $\theta = 180^\circ$. As a consequence, one of the scalar products is negative. As a result the following expression holds

$$V = 2 \frac{|\boldsymbol{\mu}|^2}{|r_{12}|^3} > 0$$

The same argument as before proves that V for this case is greater than 0.

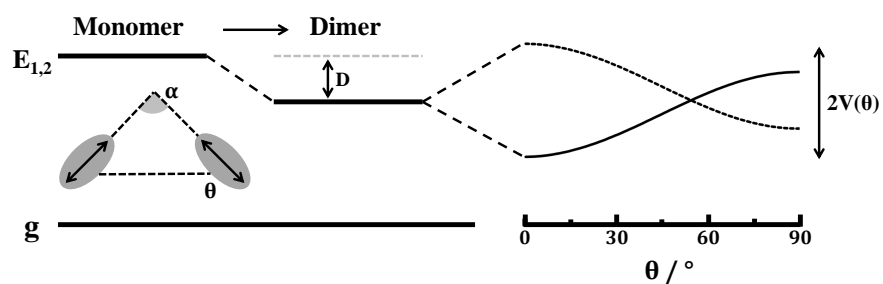


Figure 31: Arrangement of the two dipole moments and energy splitting for a coplanar configuration ($\alpha = 0^\circ$) as a function of θ . Both curves intersect for $\theta = 54.7^\circ$. Here the dotted line is dipole-forbidden, while transitions to the solid line are allowed.



Figure 32: The upper picture shows C8S3 monomers dissolved in methanol, while the picture at the bottom shows an actual sample solution after adding a sufficient amount of water to the stock solution. The redshift in absorption is clearly visible.

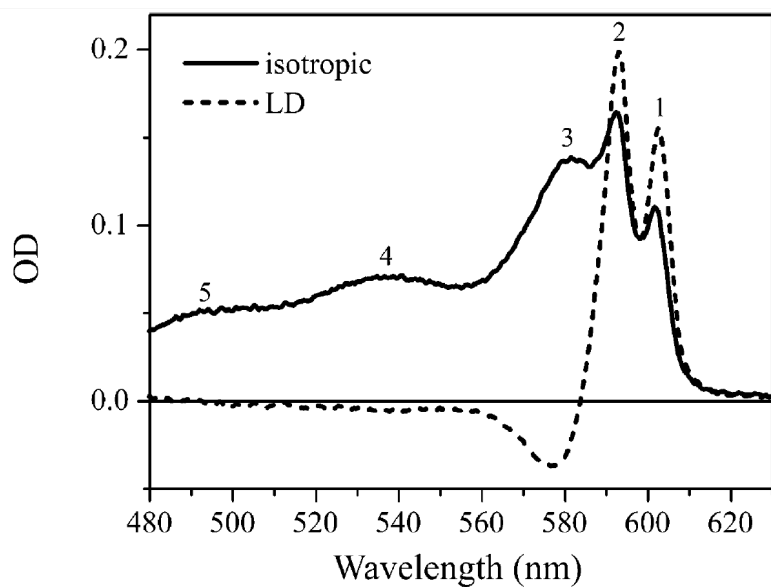


Figure 33: Isotropic absorption and linear dichroism (LD) spectra for a direct route sample solution as presented in [29]. The LD spectrum was calculated as the difference between the absorption spectra measured for light polarized parallel and perpendicular to the direction of an aligning flow.

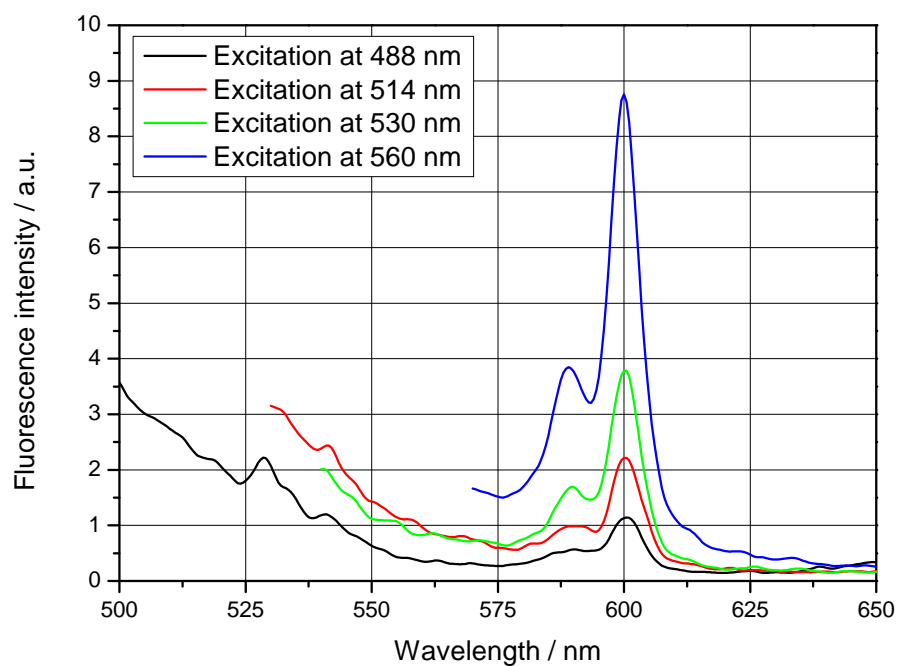


Figure 34: Fluorescence spectra as recorded at different excitation wavelengths ranging from 488 nm to 560 nm.

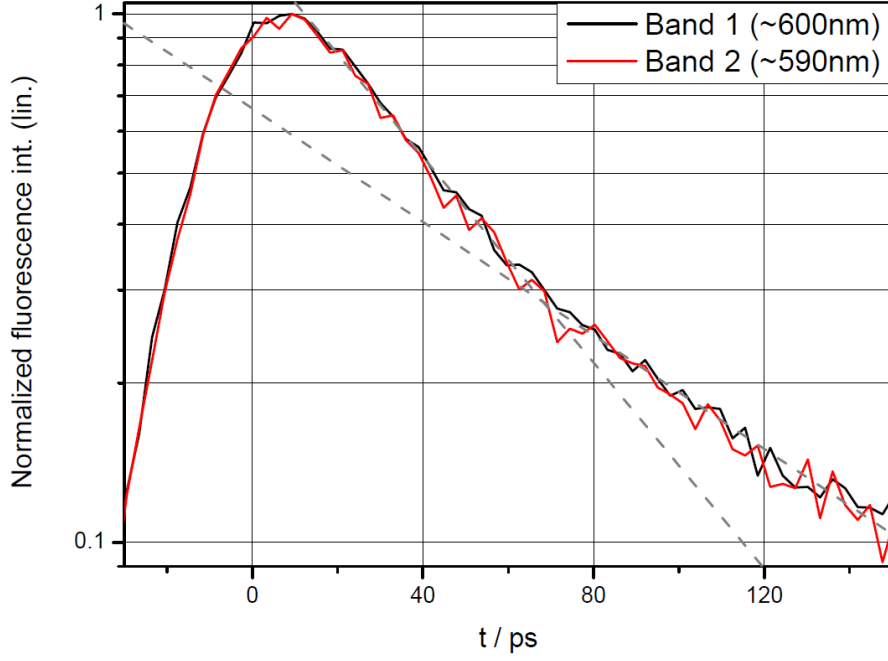


Figure 35: Zoomed in view of figure 20. The grey, dashed lines indicate the two different decay exponents.

CONVOLUTION OF A GAUSSIAN AND EXPONENTIAL FUNCTIONS

Equation 10 describes a convolution of Gaussian function and exponential functions. 10 was used to fit transients as acquired from time-resolved fluorescence measurements.

$$F(x) = \frac{1}{\sqrt{2\pi}\sigma} \int_{-\infty}^{\infty} \exp^{-\frac{t^2}{2\sigma^2}} \times \left[BL + \sum_{i=1}^N H_i \exp^{-\frac{(x-x_0)-t}{\tau_i}} \right] dt \quad (10)$$

Here, σ is the width of the Gaussian, BL the exponent baseline, H_i the height of the exponent, x_0 the peak position of the Gaussian, N the number of decaying exponents and τ_i the respective decay constants. All these were treated as fitting parameters.



Figure 36: Division of an aggregate into straight segments

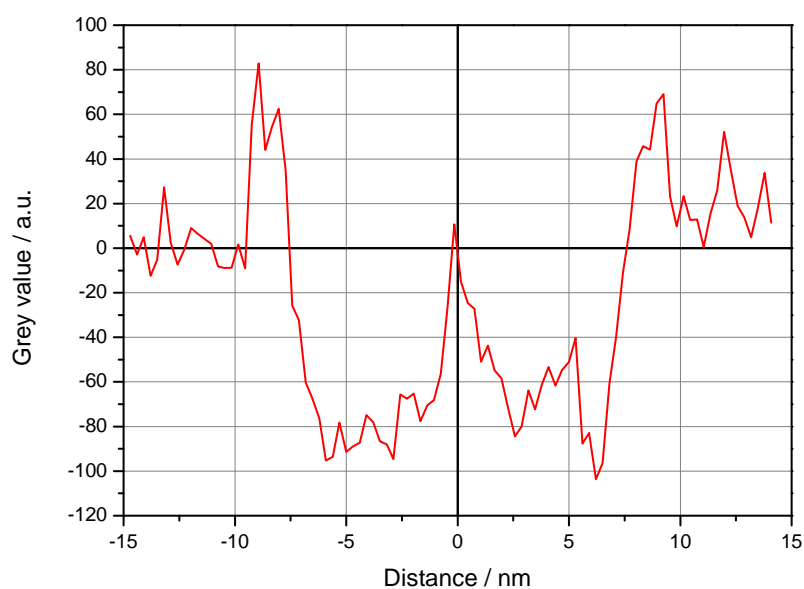


Figure 37: Exemplary line-scan of one of the segments as taken from figure 36.



Figure 38: Upon storage or due to high C8S3 concentration single aggregates form bundles, which eventually precipitate, as evident from the left cuvette. The right cuvette depicts a normal sample solution for comparison, where only a very slight degree of precipitating bundles can be observed at the bottom.

BIBLIOGRAPHY

- [1] Monthly energy review march 2015, 23/04/2015. URL http://www.eia.gov/totalenergy/data/monthly/pdf/sec1_3.pdf.
- [2] G. D. Scholes and G. Rumbles. Excitons in nanoscale systems. *Nature materials*, 5(9):683–696, 2006.
- [3] E. Collini, C. Y. Wong, K. E. Wilk, P. M. G. Curmi, P. Brumer, and G. D. Scholes. Coherently wired light-harvesting in photosynthetic marine algae at ambient temperature. *Nature*, 463(7281):644–647, 2010.
- [4] G. S. Orf and R. E. Blankenship. Chlorosome antenna complexes from green photosynthetic bacteria. *Photosynthesis research*, 116(2-3):315–331, 2013.
- [5] L. N. M. Duysens. *Transfer of excitation energy in photosynthesis*. Kemink, 1952.
- [6] V. Sundström, T. Pullerits, and R. van Grondelle. Photosynthetic light-harvesting: reconciling dynamics and structure of purple bacterial lh2 reveals function of photosynthetic unit. *The Journal of Physical Chemistry B*, 103(13):2327–2346, 1999.
- [7] R. J. Cogdell, A. T. Gardiner, H. Hashimoto, and T. H. P. Brotosudarmo. A comparative look at the first few milliseconds of the light reactions of photosynthesis. *Photochemical & Photobiological Sciences*, 7(10):1150–1158, 2008.
- [8] I. McConnell, G. Li, and G. W. Brudvig. Energy conversion in natural and artificial photosynthesis. *Chemistry & Biology Reviews*, 17(5):434–447, 2010.
- [9] A. Mishra, R. K. Behera, P. K. Behera, B. K. Mishra, and G. B. Behera. Cyanines during the 1990s: a review. *Chemical Reviews*, 100(6):1973–2012, 2000.
- [10] F. Würthner, T. E. Kaiser, and C. R. Saha-Möller. J-aggregates: From serendipitous discovery to supramolecular engineering of functional dye materials. *Angewandte Chemie International Edition*, 50(15):3376–3410, 2011.

- [11] S. Ganapathy, G. T. Oostergetel, P. K. Wawrzyniak, M. Reus, A. G. M. Chew, F. Buda, E. J. Boekema, D. A. Bryant, A. R. Holzwarth, and H. J. M. de Groot. Alternating syn-anti bacteriochlorophylls form concentric helical nanotubes in chlorosomes. *Proceedings of the National Academy of Sciences*, 106(21):8525–8530, 2009.
- [12] K. A. Clark, E. L. Krueger, and D. A. Vanden Bout. Direct measurement of energy migration in supramolecular carbocyanine dye nanotubes. *The Journal of Physical Chemistry Letters*, 5(13):2274–2282, 2014.
- [13] D. M. Eisele, J. Knoester, S. Kirstein, J. P. Rabe, and D. A. Vanden Bout. Uniform exciton fluorescence from individual molecular nanotubes immobilized on solid substrates. *Nature nanotechnology*, 4(10):658–663, 2009.
- [14] E. E. Jelley. Spectral absorption and fluorescence of dyes in the molecular state. *Nature*, 138(3502):1009–1010, 1936.
- [15] G. Scheibe. Über die veränderlichkeit der absorptionsspektren in lösungen und die nebenvalenzen als ihre ursache. *Angewandte Chemie*, 50(11):212–219, 1937.
- [16] M. Cho. *Two-dimensional optical spectroscopy*. CRC press, 2009.
- [17] D. M. Jonas. Two-dimensional femtosecond spectroscopy. *Annual review of physical chemistry*, 54(1):425–463, 2003.
- [18] G. Lanzani. *The Photophysics behind Photovoltaics and Photonics*. John Wiley & Sons, 2012.
- [19] A. McNaught, A. D. and Wilkinson. *Compendium of chemical terminology*, volume 1669. Blackwell Science Oxford, 1997.
- [20] R. M. Hochstrasser and M. Kasha. Application of the exciton model to mono-molecular lamellar systems. *Photochemistry and Photobiology*, 3(4):317–331, 1964.
- [21] A. Eisfeld and J. S. Briggs. The j-band of organic dyes: lineshape and coherence length. *Chemical physics*, 281(1):61–70, 2002.
- [22] M. Bednarz. *Dynamics of Frenkel Excitons in J-aggregates*. PhD thesis, University of Groningen, The Netherlands, 2003.

- [23] V. Malyshev and P. Moreno. Hidden structure of the low-energy spectrum of a one-dimensional localized frenkel exciton. *Physical Review B*, 51(20):14587, 1995.
- [24] S. K. Saikin, A. Eisfeld, S. Valleau, and A. Aspuru-Guzik. Photonics meets excitonics: natural and artificial molecular aggregates. *Nanophotonics*, 2(1):21–38, 2013.
- [25] E. Merzbacher. *Quantum Mechanics*. John Wiley & Sons, 1998.
- [26] J. M. Hollas. *Modern spectroscopy*. John Wiley & Sons, 2004.
- [27] W. Demtröder. *Laser Spectroscopy: Basic Concepts and Instrumentation*. Number 2674. Springer Science & Business Media, 2003.
- [28] O. Al-Khatib. *Structure and Optical Properties of Complex Aggregate-Structures of Amphiphilic Dye-Systems*. PhD thesis, Humboldt-University Berlin, Germany, 2012.
- [29] C. Didraga, A. Pugžlys, P. Hania, H. von Berlepsch, K. Duppen, and J. Knoester. Structure, spectroscopy, and microscopic model of tubular carbocyanine dye aggregates. *The Journal of Physical Chemistry B*, 108(39):14976–14985, 2004.
- [30] Jasper Knoester. Modeling the optical properties of excitons in linear and tubular j-aggregates. *International Journal of Photoenergy*, 2006, 2007.
- [31] J. Frenkel. On the transformation of light into heat in solids. i. *Physical Review*, 37(1):17, 1931.
- [32] T. Förster. Zwischenmolekulare energiewanderung und fluoreszenz. *Annalen der Physik*, 437(1-2):55–75, 1948.
- [33] R. M. Clegg. Förster resonance energy transfer-fret what is it, why do it, and how it is done. *Laboratory techniques in biochemistry and molecular biology*, 33:1–57, 2009.
- [34] A. Pawlik, A. Ouart, S. Kirstein, H. Abraham, and S. Daehne. Synthesis and uv/vis spectra of j-aggregating 5, 5, 6, 6-tetrachlorobenzimidacarbocyanine dyes for artificial light-harvesting systems and for asymmetrical generation of supramolecular helices. *European Journal of Organic Chemistry*, 2003(16):3065–3080, 2003.

- [35] H. von Berlepsch, K. Ludwig, S. Kirstein, and C. Böttcher. Mixtures of achiral amphiphilic cyanine dyes form helical tubular j-aggregates. *Chemical Physics*, 385(1):27–34, 2011.
- [36] V. V. Prokhorov, E. I. Maltsev, O. M. Perelygina, D. A. Lypenko, S. I. Pozin, and A. V. Vannikov. High precision nanoscale afm height measurements of j-aggregates. *Nanotechnologies in Russia*, 6(5-6):286–297, 2011.
- [37] V. Czikkely, H. D. Försterling, and H. Kuhn. Light absorption and structure of aggregates of dye molecules. *Chemical Physics Letters*, 6(1):11–14, 1970.
- [38] H. Von Berlepsch, S. Kirstein, and C. Böttcher. Effect of alcohols on j-aggregation of a carbocyanine dye. *Langmuir*, 18(20):7699–7705, 2002.
- [39] H. von Berlepsch, S. Kirstein, R. Hania, A. Pugzlys, and C. Böttcher. Modification of the nanoscale structure of the j-aggregate of a sulfonate-substituted amphiphilic carbocyanine dye through incorporation of surface-active additives. *The Journal of Physical Chemistry B*, 111(7):1701–1711, 2007.
- [40] S. Kirstein and S. Daehne. J-aggregates of amphiphilic cyanine dyes: Self-organization of artificial light harvesting complexes. *International Journal of Photoenergy*, 2006, 2007.
- [41] D. M. Eisele, D. H. Arias, X. Fu, E. A. Bloemsma, C. P. Steiner, R. A. Jensen, P. Rebentrost, H. Eisele, A. Tokmakoff, S. Lloyd, et al. Robust excitons inhabit soft supramolecular nanotubes. *Proceedings of the National Academy of Sciences*, 111(33):E3367–E3375, 2014.
- [42] C. Spitz, J. Knoester, A. Ouart, and S. Daehne. Polarized absorption and anomalous temperature dependence of fluorescence depolarization in cylindrical j-aggregates. *Chemical physics*, 275(1):271–284, 2002.
- [43] D. M. Eisele, C. W. Cone, E. A. Bloemsma, S. M. Vlaming, C. G. F. van der Kwaak, R. J. Silbey, M. G. Bawendi, J. Knoester, J. P. Rabe, and D. A. Vanden Bout. Utilizing redox-chemistry to elucidate the nature of exciton transitions in supramolecular dye nanotubes. *Nature chemistry*, 4(8):655–662, 2012.

- [44] S. Kirstein, H. von Berlepsch, and C. Böttcher. Photo-induced reduction of noble metal ions to metal nanoparticles on tubular j-aggregates. *International Journal of Photoenergy*, 2006, 2007.
- [45] A. Pugžlys, R. Augulis, P. H. M. Van Loosdrecht, C. Didraga, V. A. Malyshev, and J. Knoester. Temperature-dependent relaxation of excitons in tubular molecular aggregates: fluorescence decay and stokes shift. *The journal of physical chemistry B*, 110(41):20268–20276, 2006.
- [46] R. Augulis, A. Pugžlys, and P. H. M. van Loosdrecht. Exciton dynamics in molecular aggregates. *physica status solidi (c)*, 3(10):3400–3403, 2006.
- [47] L. Reimer and H. Kohl. *Transmission electron microscopy: physics of image formation*, volume 36. Springer Science & Business Media, 2008.
- [48] J. Megow, M. I. S. Röhr, M. Schmidt am Busch, T. Renger, R. Mitrić, S. Kirstein, J. Rabe, and V. May. Site-dependence of van der waals interaction explains exciton spectra of double-walled tubular j-aggregates. *Physical Chemistry Chemical Physics*, 2015.
- [49] H. von Berlepsch, S. Kirstein, and C. Böttcher. Controlling the helicity of tubular j-aggregates by chiral alcohols. *The Journal of Physical Chemistry B*, 107(36):9646–9654, 2003.
- [50] H. Von Berlepsch, C. Böttcher, A. Quart, C. Burger, S. Daehne, and S. Kirstein. Supramolecular structures of j-aggregates of carbocyanine dyes in solution. *The Journal of Physical Chemistry B*, 104(22):5255–5262, 2000.
- [51] M. N. Wallack. Investigations of the c8s3 aggregate. Master’s thesis, University of Texas at Austin, USA, 2012.
- [52] F. Milota, V. I. Prokhorenko, T. Mancal, H. von Berlepsch, O. Bixner, H. F. Kauffmann, and J. Hauer. Vibronic and vibrational coherences in two-dimensional electronic spectra of supramolecular j-aggregates. *The Journal of Physical Chemistry A*, 117(29):6007–6014, 2013.
- [53] J. Sperling, A. Nemeth, J. Hauer, D. Abramavicius, S. Mukamel, H. F. Kauffmann, and F. Milota. Excitons and disorder in molecular nanotubes: a 2d electronic spectroscopy study and first comparison to a microscopic

- model. *The Journal of Physical Chemistry A*, 114(32):8179–8189, 2010.
- [54] J. Lim, D. Paleček, F. Caycedo-Soler, C. N. Lincoln, J. Prior, H. von Berlepsch, S. F. Huelga, M. B. Plenio, D. Zigmantas, and J. Hauer. Verification of the vibronic origin of long-lived coherence in an artificial molecular light harvester. *arXiv preprint arXiv:1502.01717*, 2015.
- [55] G. Cerullo, M. Nisoli, and S. De Silvestri. Generation of 11 fs pulses tunable across the visible by optical parametric amplification. *Applied physics letters*, 71(25):3616–3618, 1997.
- [56] A. Shirakawa, I. Sakane, M. Takasaka, and T. Kobayashi. Sub-5-fs visible pulse generation by pulse-front-matched noncollinear optical parametric amplification. *Applied physics letters*, 74(16):2268–2270, 1999.
- [57] M. Bradler, P. Baum, and E. Riedle. Femtosecond continuum generation in bulk laser host materials with sub- μ j pump pulses. *Applied Physics B*, 97(3):561–574, 2009.

DECLARATION

I declare that I have developed and written the enclosed Master Thesis completely by myself, and have not used sources or means without declaration in the text. Any thoughts from others or literal quotations are clearly marked. The Master Thesis was not used in the same or in a similar version to achieve an academic grading or is being published elsewhere.

Groningen, June 2015

Björn Kriete